Volume 74, Number 23   December 1, 2010

Articles

Effects of changing solution chemistry on Fe^{3+}/Fe^{2+} isotope fractionation in aqueous Fe–Cl solutions

Pamela S. Hill [a,*], Edwin A. Schauble [a], Edward D. Young [a,b]

[a] Department of Earth and Space Sciences, University of California, Los Angeles, CA 90095, USA
[b] Institute of Geophysics and Planetary Physics, University of California, Los Angeles, CA 90095, USA

Abstract

The range in $^{56}Fe/^{54}Fe$ isotopic compositions measured in naturally occurring iron-bearing species is greater than 5‰. Both theoretical modeling and experimental studies of equilibrium isotopic fractionation among iron-bearing species have shown that significant fractionations can be caused by differences in oxidation state (i.e., redox effects in the environment) as well as by bond partner and coordination number (i.e., nonredox effects due to speciation).

To test the relative effects of redox vs. nonredox attributes on total Fe equilibrium isotopic fractionation, we measured changes, both experimentally and theoretically, in the isotopic composition of an Fe^{2+}–Fe^{3+}–Cl–H_2O solution as the chlorinity was varied. We made use of the unique solubility of $FeCl_4^-$ in immiscible diethyl ether to create a separate spectator phase against which changes in the aqueous phase could be quantified. Our experiments showed a reduction in the redox isotopic fractionation between Fe^{2+}- and Fe^{3+}-bearing species from 3.4‰ at $[Cl^-] = 1.5$ M to 2.4‰ at $[Cl^-] = 5.0$ M, due to changes in speciation in the Fe–Cl solution. This experimental design was also used to demonstrate the attainment of isotopic equilibrium between the two phases, using a ^{54}Fe spike.

To better understand speciation effects on redox fractionation, we created four new sets of ab initio models of the ferrous chloride complexes used in the experiments. These were combined with corresponding ab initio models for the ferric chloride complexes from previous work. At 20 °C, $1000 \ln \beta$ ($\beta = {}^{56}Fe/^{54}Fe$ reduced partition function ratio relative to a dissociated Fe atom) values range from 6.39‰ to 5.42‰ for $Fe(H_2O)_6^{2+}$, 5.98‰ to 5.34‰ for $FeCl(H_2O)_5^+$, and 5.91‰ to 4.86‰ for $FeCl_2(H_2O)_4$, depending on the model. The theoretical models predict ferric–ferrous fractionation about half as large (depending on model) as the experimental results.

Our results show (1) oxidation state is likely to be the dominant factor controlling equilibrium Fe isotope fractionation in solution and (2) nonredox attributes (such as ligands present in the aqueous solution, speciation and relative abundances, and ionic strength of the solution) can also have significant effects. Changes in the isotopic composition of an Fe-bearing solution will influence the resultant Fe isotopic signature of any precipitates.
© 2010 Elsevier Ltd. All rights reserved.

1. INTRODUCTION

Large variations in isotopic composition ($^{56}Fe/^{54}Fe$) among iron-bearing species in geological and biological systems at Earth-surface temperatures (from $\delta^{56}Fe = -3.6‰$ (sedimentary pyrite) to 1.6‰ (Fe-oxide in banded-iron formation)) have been found in natural samples (e.g., Beard and Johnson, 2004, and references therein; Rouxel et al., 2005; Hofmann et al., 2009), laboratory experiments (e.g., Anbar et al., 2000; Johnson et al., 2002; Welch et al., 2003), and in theoretical models (e.g., Polyakov and Mineev, 2000; Schauble et al., 2001; Anbar et al., 2005; Hill and Schauble, 2008). Such variations have primarily been attributed to redox effects in the environment upon fractionations among iron-bearing species, suggesting that $^{56}Fe/^{54}Fe$ may be an indicator of past oxygen fugacity levels

---

* Corresponding author.
  E-mail address: phill@ess.ucla.edu (P.S. Hill).

in the sedimentary record (e.g., Rouxel et al., 2005; Yamaguchi and Ohmoto, 2006; Yamaguchi et al., 2007) and/or of bacterial processes (e.g., Johnson et al., 2008, and references therein).

However, theoretical studies (Polyakov and Mineev, 2000; Schauble et al., 2001; Liu and Tang, 2006; Tang and Liu, 2007; Domagal-Goldman and Kubicki, 2008; Hill and Schauble, 2008) and experimental studies (Fujii et al., 2006; Hill et al., 2009) indicate that changes in the nonredox bond environment (i.e., different ligands or coordination numbers) should also result in significant equilibrium isotopic fractionation among iron-bearing species. In earlier studies we demonstrated the effects of both coordination number and bond partner on fractionation among ferric chloride complexes in aqueous solutions by developing and comparing ab initio models for ferric chloride species (Hill and Schauble, 2008) and by conducting experiments on fractionation among aqueous Fe^{3+}–Cl complexes as the solution chemistry was varied (Hill et al., 2009). In the experiments, changes in the isotopic fractionation between an aqueous solution of ferric chloride complexes ($Fe(H_2O)_6^{3+}$ to $FeCl_4^-$) and a spectator phase ($FeCl_4^-$ dissolved in ether) were measured as the chlorinity of the solution was increased. As would be expected, speciation models showed that the relative abundances of the ferric chloride complexes change as the chlorinity of the solution changes; this, in turn, was observed to alter the isotopic fractionation between the aqueous and ether phases. Our experimental data showed an average decrease in iron isotope fractionation of $\sim 0.18‰$/M Cl$^-$ (from 0.5 to 5.0 M Cl$^-$ at a constant ionic strength of ~ 5) between the aqueous and ether phases. Our theoretical models predicted a similar decrease in iron fractionation between the aqueous and ether phases of 0.16–0.22‰/M Cl$^-$ (depending on the model method and basis set—see Section 2.4).

In this work we investigate the relative effects of redox vs. nonredox attributes on $^{56}Fe/^{54}Fe$ fractionation via: (1) new experiments that combine aqueous ferric and ferrous chloride complexes under varying solution chemistries and (2) new ab initio models of the ferrous chloride complexes, which we combine with ab initio models of the ferric chloride complexes (developed in Hill and Schauble, 2008). The Fe–Cl complexes of interest are detailed in Table 1, including the species abbreviations used hereafter.

We adapted the same two-phase experimental design used in our ferric chloride experiments (detailed in Hill et al., 2009), this time employing an aqueous phase containing both ferric chloride and ferrous chloride complexes and an ether phase containing $FeCl_4^-$ (the only Fe–Cl complex dissolvable in ether (Nachtrieb and Conway, 1948)). Key to the experimental design is the change in the relative abundances of the Fe–Cl complexes as the chlorinity of the aqueous solution changes, resulting in different combinations of bonding partners, coordination numbers, and oxidation states.

The ether serves as a spectator phase against which changes in isotopic fractionation among the Fe–Cl complexes in the aqueous phase can be quantified, as the chlorinity of the aqueous solution is varied. The ether phase is easily equilibrated with the aqueous phase, and can be

Table 1
Ferric and ferrous chloride complexes, abbreviations, and geometries.

Complex	Abbreviation (# Cl atoms)	# Fe–Cl bonds	Charge	Structure
Ferric				
$Fe(H_2O)_6^{3+}$	**C0**	0	+3	Octahedral
$FeCl(H_2O)_5^{2+}$	**C1**	1	+2	Octahedral
$FeCl_2(H_2O)_4^+$	**C2**	2	+1	Octahedral (*trans*)
$FeCl_3(H_2O)_3$	**C3**	3	0	Octahedral (*fac*)
$FeCl_4^-$	**C4**	4	−1	Tetrahedral
Ferrous				
$Fe(H_2O)_6^{2+}$	**D0**	0	+2	Octahedral
$FeCl(H_2O)_5^+$	**D1**	1	+1	Octahedral
$FeCl_2(H_2O)_4$	**D2**	2	0	Octahedral (*trans*)

quantitatively separated from that solution without disturbing the equilibrium. The two-phase design is also used in a reversal experiment to show that the experiments reach isotopic equilibrium within a reasonable time (60 min).

The geochemical importance of these experiments lies mainly in their potential generalization to other iron-ligand systems in which changing speciation under different aqueous conditions might bring about changes in the overall isotope signature. The results of our studies of the Fe–Cl system should be expandable to other Fe systems found in nature, such as sulfides, small organic ligands, and siderophores, but which are more difficult to study at equilibrium in the lab. By necessity in the experimental design, the chlorinity of our experiments is higher and the pH lower than that found in most natural systems. However, it is worth pointing out that Fe–Cl complexes do occur naturally in some oxidized, low-pH or highly saline fluids, such as sulfate-chloride lakes near volcanoes, evaporative basins, and mine runoff, and that they can coexist with Fe–S species. Though uncommon on Earth today, these environments are of intrinsic interest as potential habitats for extremophiles, and as terrestrial analogs for Mars (e.g., Delmelle and Bernard, 1994; Jamieson et al., 2005; Tosca et al., 2005; Amils et al., 2007; Bowen et al., 2007).

Further, the experimental techniques developed in these studies can be potentially expanded to measure fractionations associated with small, labile organic ligands analogous to biological molecules and more broadly to measurements of species-dependent isotopic fractionations of other elements in solution.

2. THEORY AND METHODS

2.1. The ferric and ferrous chloride complexes

The major complexes in an acidic aqueous solution of ferric chloride at room temperature ($\sim 20\,°C$) are $Fe(H_2O)_6^{3+}$, $Fe(H_2O)_5Cl^{2+}$, $Fe(H_2O)_4Cl_2^+$, $Fe(H_2O)_3Cl_3$, and $FeCl_4^-$ (Table 1), according to spectroscopic studies (e.g., Lind, 1967; Cotton and Gibson, 1971; Sharma,

1974; Best et al., 1984; Murata and Irish, 1988; Murata et al., 1989). Further complexing may produce the species FeCl$_5$(H$_2$O)$^{2-}$ and FeCl$_6^{3-}$ (Shamir, 1991; Inada and Funahashi, 1999), but in abundances too small to be significant in these experiments. Ferric hydroxide complexes are also considered negligible due to the low-pH of the solutions (−1 to 0). In accordance with the abbreviation convention used in Hill and Schauble (2008), we will refer to these complexes according to the number of Fe–Cl bonds as follows: **C0** = Fe(H$_2$O)$_6^{3+}$, **C1** = (Fe(H$_2$O)$_5$Cl)$^{2+}$, etc. (see Table 1).

The major ferrous chloride complexes at room temperature ($\sim$20 °C) in an aqueous acidic solution are Fe(H$_2$O)$_6^{2+}$, Fe(H$_2$O)$_5$Cl$^+$, and Fe(H$_2$O)$_4$Cl$_2$ (e.g., Heinrich and Seward, 1990; Zhao and Pan, 2001; Liu et al., 2007). FeCl$_4^{2-}$ appears at significant concentrations only at much higher temperatures and chlorinities than used in our experiments (Zhao and Pan, 2001; Liu et al., 2007). Following the naming convention for ferric chlorides above, we have abbreviated the ferrous chloride complexes as **D0** = Fe(H$_2$O)$_6^{2+}$, **D1** = (Fe(H$_2$O)$_5$Cl)$^+$, and **D2** for (Fe(H$_2$O)$_4$Cl$_2$) (Table 1).

C0, **C1**, and **C2** have octahedral geometries; **C4** is tetrahedral (Magini and Radnai, 1979; Apted et al., 1985). There is some uncertainly whether the structure of **C3** is octahedral or trigonal bipyramidal (Lind, 1967; Bjerrum and Lukes, 1986). In a previous work we created ab initio models for all the ferric chloride complexes (Hill and Schauble, 2008). We used those models when calculating the theoretical predications for our current experiments; **C3** was modeled as octahedral *fac* (i.e., with Cl$^-$ ions on the three corners of one face of the octahedron). The ferrous chloride structures **D0**, **D1**, and **D2** are basically octahedral in geometry, but have minor Jahn–Teller distortion in their minimum potential-energy configurations due to the unequal occupancy of the d orbitals.

2.2. Experimental procedures

2.2.1. Overview of experimental design

In previous work (Hill et al., 2009), we measured the changes in Fe isotope fractionation among the ferric chloride complexes in a ferric chloride solution resulting from increases in chlorinity. We used a similar two-phase (aqueous–ether) experimental setup in the present study. We added ferrous chloride in varying amounts to the ferric chloride solution and then measured the resulting changes in ^{56}Fe/^{54}Fe fractionation between the ferric and the ferrous species.

Another important difference in the experimental setup between the new experiments (this work) and the previous experiments (Hill et al., 2009) is that the ionic strength of the solution in the previous experiments was held constant ($\sim$5) by the addition of appropriate amounts of nitric acid; the ionic strength in the new experiments increases ($\sim$1–5) as chlorinity increases; no nitric acid is added because it is incompatible with Fe^{2+} aq. This difference alters the speciation abundances vs. chlorinity relationships slightly and affects the magnitude of the overall change in fractionation (Section 3.3).

2.2.2. Definition of terms

The per mil Fe isotopic composition δ^{56}Fe of a sample relative to a standard is defined as

$$\delta^i \text{Fe} = 10^3 \left(\frac{(^i\text{Fe}/^{54}\text{Fe})_{Sample}}{(^i\text{Fe}/^{54}\text{Fe})_{Std}} - 1 \right) \qquad (1)$$

where i is either 56 or 57, *Std* represents an in-house Fe isotope standard, and *Sample* signifies the sample. Isotope ratios in this work are reported as δ^{56}Fe and δ^{57}Fe relative to an in-house standard Spex-1; the isotopic composition of this standard is related to the IRMM-14 iron standard by the experimentally determined δ^{56}Fe(IRMM-14) = δ^{56}Fe(Spex-1) − 0.21‰ (Hill et al., 2009).

The per mil Fe fractionation $1000 \ln \alpha_{(AX-BX)}$ between two samples AX and AB is calculated as

$$1000 \ln \alpha_{(AX-BX)} \approx \delta^{56}\text{Fe}_{AX} - \delta^{56}\text{Fe}_{BX} \text{ for } \alpha \approx 1 \qquad (2)$$

We define the fractionation between the aqueous and ether phases as $\Delta^{56}\text{Fe}_{(aq-eth)}$ where

$$\Delta^{56}\text{Fe}_{(aq-eth)} = \delta^{56}\text{Fe}_{aq} - \delta^{56}\text{Fe}_{eth} \qquad (3)$$

where $\delta^{56}\text{Fe}_{aq}$ is the ^{56}Fe/^{54}Fe per mil composition of the aqueous phase; and $\delta^{56}\text{Fe}_{eth}$, the ^{56}Fe/^{54}Fe the per mil composition of the ether phase.

We then define the fractionation between the ferric species and the ferrous species, α (Fe^{3+}–Fe^{2+}) for a given chlorinity, as the difference between the aqueous–ether fractionation of a solution of all-ferric complexes and the aqueous–ether fractionation of a solution of all-ferrous complexes, such that

$$1000 \ln \alpha(\text{Fe}^{3+}\text{–Fe}^{2+}) = \Delta^{56}\text{Fe}_{(aq-eth)} (\text{all Fe}^{3+}\text{–Cl aq solution})$$
$$- \Delta^{56}\text{Fe}_{(aq-eth)} (\text{all Fe}^{2+}\text{–Cl aq solution}). \qquad (4)$$

Fe^{2+}/Fe$_{total}$ = 1 represents an all-ferrous solution; Fe^{2+}/Fe$_{total}$ = 0, an all-ferric solution. [Fe$_{total}$] = [Fe$_{ferric}$] + [Fe$_{ferrous}$][1] (see Section 2.2.8 for computational details).

The reduced partition function ratio, β_{56-54} (AX–X), (hereafter denoted as β), calculated from the ab initio models, is the theoretical ^{56}Fe/^{54}Fe fractionation between an iron-bearing phase AX and a dissociated monatomic gas of X (Fe) atoms at equilibrium. It is reported in per mil as $1000 \ln \beta$; calculation details are given in Appendix A.1.1.

2.2.3. Aqueous phase

Aqueous solutions (20 ml) containing both ferric chloride and ferrous chloride were created with chlorinities of 1.5 M, 2.5 M, 4.0 M, and 5.0 M Cl$^-$. At 1.5 M, 2.5 M, and 5.0 M, we mixed a series of four solutions, each with a different initial molar ratio of ferric to ferrous iron (100:0, 75:25, 50:50, and 25:75). At 4.0 M, we mixed a series of three solutions, with initial molar ratios of ferric to ferrous iron of 100:0, 65:35, and 25:75. Total initial aqueous [Fe] was calculated to be 0.15 M.

---

[1] [Y] represents the molar concentration (mole/liter) of a species Y in solution.

Stock solutions of ferric chloride were prepared from powdered hematite, iron(III) oxide (Fe_2O_3) and 12-M reagent grade HCl. The hematite was 99.9995+ % pure, in order to avoid contamination by Cr in the MC-ICP-MS (see Section 2.2.7). The mixture was heated in a closed Teflon Savillex™ beaker on a hot plate at about 100 °C for about 12 h until all the hematite powder was dissolved, resulting in an aqueous solution of Fe^{3+}-Cl complexes. We found it necessary to use about twice as much HCl as might be expected stoichiometrically in order to dissolve all the hematite. We let the mixture cool and then added deionized water and/or additional HCl to achieve the desired chloride and iron concentrations.

Stock solutions of ferrous chloride were prepared with crystals of iron(II) chloride tetrahydrate, $FeCl_2·4(H_2O)$, 99+ % pure. Analyses indicate that contamination with Cr is not an issue with $FeCl_2·4(H_2O)$ reagent. To avoid oxidation of the ferrous chloride stock solution over the course of an experiment, new ferrous chloride stock was mixed up fresh each day in a solution of 1.0 M HCl. Concentrations of both Fe^{2+} and total Fe in the stock solution were measured before and after each day's experiments (see Section 2.2.6); no oxidation of the ferrous iron was detected over the course of a day. The additional HCl was taken into account in the calculations of total hydrogen and chloride in the aqueous solution.

The ferrous chloride and ferric chloride stock solutions were mixed together in the desired ratio for each experiment's aqueous solution. Additional HCl and deionized water were added as needed to control the total chloride concentration. Hence, both $[H^+]$ and the total ionic strength of the solution increased with $[Cl^-]$ (pH remained <0). $[H^+]$ was always slightly less than $[Cl^-]$ since some $[Cl^-]$ also comes from the original $FeCl_2·4(H_2O)$, (i.e., $[H^+] = [Cl^-] - 2 * [Fe^{2+}]$) (except in the all-ferric solutions). All measurements were made with an Eppendorf™ auto-pipette. The solutions were gently shaken and then allowed to rest for 10 min in a separation funnel (Fig. A1).

As an additional check on possible oxidation of the ferrous chloride species, we measured the initial and final concentrations of Fe^{2+} and total Fe in a mixture of ferric and ferrous chlorides (with no ether added) left to rest for several hours, but detected no change in Fe^{2+}.

2.2.4. Ether phase

An equal volume (20 ml) of immiscible diethyl ether was added to the aqueous solution using a 25 ml graduated glass cylinder. The mixture was shaken briskly, and then left to rest, covered, for at least 60 min. The ether formed a separate liquid phase on top of the aqueous phase. During this time, some aqueous $FeCl_4^-$ dissolved into the ether, turning it various shades of yellow to brownish yellow, depending on the iron concentration (Fig. A1). A very small portion of $FeCl_4^-$ also remained in the aqueous phase.

C4 is the only iron chloride species dissolvable in ether and is most likely extracted into the ether as stoichiometric $HFeCl_4$ (i.e., $FeCl_4^-·H_3O^+·nH_2O$). The amount of **C4** dissolved into the ether rises very rapidly with increasing $[Cl^-]$ and $[H^+]$ (Dodson et al., 1936; Sandell, 1944;

Nachtrieb and Fryxell, 1948; Hill et al., 2009) (see Section 3.1).

2.2.5. Separation of phases

Separate aliquots of the aqueous (0.25 ml) and ether (1 ml) phases were removed immediately following the rest period to Savillex™ beakers for isotopic analysis, without disturbing the equilibrium of the mixture. Ethereal samples were taken from the top of the funnel by a disposable pipette (with gradations of 0.25 ml). A few milliliters of aqueous solution were allowed to run through the stopcock at the bottom of the funnel; then some aqueous solution was gathered from the stopcock in a glass beaker, from which sample measurements were taken with an auto-pipette. One milliliter of 1.0 M HCl was added to each ether sample to ensure aqueous re-dissolution of all iron as the ether evaporated. Samples were dehydrated on a hot plate (100 °C for aqueous samples; 50 °C for ether samples) to remove HCl, and then rehydrated with dilute nitric acid. Samples were further diluted with 2% nitric acid to match the concentration of the iron isotope standard used for mass spectrometry. (By the time the ferrous samples are dried down and rehydrated, they have most likely oxidized, thus eliminating adverse ferrous-nitric acid interactions.)

2.2.6. Fe concentration measurements

Ferrous and total iron concentrations (total = ferric + ferrous) in the aqueous phase and total iron (ferric) concentrations in the ether phase for each sample were determined on a GENESYS20 spectrophotometer using the standard ferrozine method (Stookey, 1970; Vollier et al., 2000; detailed in Hill et al., 2009). Ferric iron was reduced to ferrous iron with hydroxylamine hydrochloride for total iron determinations.

Since some ferric iron is extracted from the aqueous solution by dissolution into the ether phase, the ratio of ferric to ferrous iron in the aqueous phase at the end of the experiment is smaller than the initial ratio. Initial ratios of ferric to ferrous iron in the aqueous solution were measured immediately after combining the ferric chloride and ferrous chloride and before the addition of ether to the aqueous solution (to ensure no oxidation of ferrous iron was occurring). Final ratios of ferric to ferrous iron in the aqueous solution were measured after the ether–aqueous solution was allowed to rest for at least 60 min. It is these final ratios that are used in the calculations of $\Delta^{56}Fe_{(aq-eth)}$ (all Fe^{2+}–Cl aq solution) (see Eq. (4) and Section 2.2.8).

2.2.7. Isotopic measurements and aqueous–ether fractionations ($\Delta^{56}Fe_{(aq-eth)}$)

Isotope ratios $^{56}Fe/^{54}Fe$ and $^{57}Fe/^{54}Fe$ of the ether and aqueous aliquots for each sample were measured on the UCLA Thermo Finnigan Neptune MC-ICP-MS (Multiple Collector Inductively Coupled Plasma Mass Spectrometer). No $^{52}Cr^+$ was detected in the solutions, eliminating the possibility of interference from $^{54}Cr^+$. Samples consisted of pure Fe in dilute nitric acid and were run in dry plasma using a desolvating nebulizer (Celac Aridus) as ~1 ppm Fe in ~2% HNO_3. Standard-sample-standard bracketing was used to correct for instrumental mass bias.

Iron isotope fractionation between aqueous Fe and ethereal $FeCl_4^-$ is expressed as $\Delta^{56}Fe_{(aq-eth)}$ (Eq. (3)). Values for $\Delta^{56}Fe_{(aq-eth)}$ were determined for aqueous–ether pairs of each molarity of Cl^- and each ratio of $Fe^{2+}/Fe_{total\ aq}$ where $Fe_{total\ aq}$ is the total iron concentration (ferric + ferrous) in the aqueous phase.

2.2.8. Final Fe^{3+}/Fe^{2+} isotopic fractionation measurements: $1000\ ln\ \alpha\ (Fe^{3+}-Fe^{2+})$

Ferric–ferrous fractionations in aqueous solution are calculated from the all-ferric and all-ferrous $\Delta^{56}Fe_{(aq-eth)}$ (Eq. (4)). The all-ferric $\Delta^{56}Fe_{(aq-eth)}$ (all Fe^{3+}–Cl aq solution) is obtained directly from the appropriate experiment (Eq. (3)).

However, the all-ferrous $\Delta^{56}Fe_{(aq-eth)}$ cannot be measured directly since no Fe^{2+} complex is soluble in ether. In order to determine the fractionation of an all Fe^{2+} aqueous phase relative to the ether phase, we measured the aqueous–ether fractionation for a series of solutions with different ratios of Fe^{2+} and Fe^{3+} at a given chlorinity. Using the final $Fe^{2+}/Fe_{total\ aq}$ ratios measured at the end of the ether rest time (see Section 2.2.6), we extrapolated the best-fit line for measured $\Delta^{56}Fe_{(aq-eth)}$ vs. $Fe^{2+}/Fe_{total\ aq}$ using a modified York regression[2] (Mahon, 1996) of $\Delta^{56}Fe_{(aq-eth)}$. $\Delta^{56}Fe_{(aq-eth)}$ for all-ferrous solution ($Fe^{2+}/Fe_{total\ aq} = 1$) is determined from the y-intercept of the best-fit line[3].

2.3. Reversal experiments (demonstration of isotopic equilibrium)

Evidence for the attainment of mass-dependent, isotope-exchange equilibrium in the aqueous system comes from the use of a two-phase aqueous/ether system, an isotope spike (^{54}Fe), and portrayal of the data in three-isotope space[4] (Mathews et al., 1983; Shahar et al., 2008; detailed in Hill et al., 2009). One signature of equilibrium is that the same point (in this case, $\Delta^{56}Fe_{(aq-eth)}$) is approached from two opposing disequilibrium starting conditions (forward and reverse). In our forward experiments, iron is transferred from the aqueous phase to the ether phase (as unspiked **C4**); in the reversal experiment, ether containing spiked **C4** ($^{54}FeCl_4^-$) from one completed forward experiment is added to the ether of a second unspiked, completed, forward experiment. This forces net transport of the spiked **C4** in the ether to the aqueous phase, resulting ultimately (in the equilibrium case) in the same isotopic partitioning.

Attainment of isotopic equilibrium is thus inferred from three necessary criteria. Any one of these criteria is a necessary condition of equilibrium but, as in any exchange experiment, none taken alone is sufficient to prove equilibrium. First, both phases initially lying on distinctive mass fractionation lines come to rest on a single SFL, demonstrating complete mass-dependent isotope exchange such that $\alpha^{56/54} = (\alpha^{57/54})^\gamma$ where $\gamma = (1/m_{54} - 1/m_{56})/(1/m_{54} - 1/m_{57})$ and where m_i = mass of isotope i (Matsuhisa et al., 1978; Young et al., 2002). Second, As the solutions exchange isotopes, each phase moves along a linear mixing line toward a distinct and reproducible isotopic composition on the SFL (i.e., the intersection point of the mixing line with the SFL). Third, both the forward and the reversal experiment yield the same $\Delta^{56}Fe_{(aq-eth)}$, within experimental error (see Fig. 7). Satisfying all three of these criteria, especially #3, is consistent with the achievement of isotope-exchange equilibrium.

To prepare the spiked ether needed for the reversal experiment, two forward experiments were run simultaneously, with $[Cl^-] = 3.0\ M$ and initial $Fe^{2+}/Fe_{total\ aq} = 0.5$, one with a normal isotope content and one prepared with aqueous $^{54}Fe^{3+}$ spike. Once the mixtures were believed to have achieved equilibrium (60 min), half the ether (10 ml) from the spiked experiment (containing excess $^{54}FeCl_4^-$) was added to the ether of the normal-isotope forward experiment, creating the reversal experiment starting at time $t = 0$ s, with 20 ml aqueous phase and 30 ml ether phase. The rate and progress of the reversal experiment toward equilibrium were measured by removing small aliquots from both the ether and aqueous phases after 20, 40, 60 min and then at 36 h[5] (without disturbing the mixtures). Measured Fe isotope compositions were then plotted in three-isotope space. The iron concentration in each phase was measured at 60 min in order to calculate the bulk isotopic composition of the mixture.

2.4. Theoretical modeling of ferric–ferrous fractionation

2.4.1. Ab initio models of the ferrous chloride complexes

Four sets of theoretical models for equilibrium isotopic fractionation were created using two different ab initio methods, Unrestricted Hartree Fock (UHF) and hybrid Density Functional Theory (DFT), B3LYP (Becke, 1993), paired with different basis sets, using Gaussian 03 (Frisch et al., 2004). Each model produces a set of molecular vibrational frequencies for each isotopic form of interest, from which the β factors can be calculated. The four sets of ferrous chloride ab initio models developed for this work

---

[2] The York regression was used since both the x and y variables are subject to error.

[3] $1000\ ln\ \alpha\ (Fe^{3+}-Fe^{2+})$ can also be calculated directly from the slope of the best-fit line since it represents the vertical distance along the ordinate axis for a corresponding distance of 1 along the abscissa.

[4] In three-isotope space ($\delta^{56}Fe$ vs. $\delta^{57}Fe$) mass-dependent iron-bearing terrestrial species lie along the terrestrial fractionation line (TFL). The spiked ether phase will lie below the TFL due to excess ^{54}Fe. Isotopic exchange between the ether phase and the unspiked aqueous phase will establish equilibrium along a secondary fractionation line (SFL), below and parallel to the TFL, that passes through the bulk isotopic composition of the system.

[5] The 36-h measurements were not part of the original experimental design. After completion of the 60-min reversal experiment, the separation funnel was unintentionally left uncovered in the fume hood with no other modifications. Out of curiosity 36 h later, we took an isotopic sample. The 36-h results are also shown but may be suspect due to the possible evaporation of some ether and possible oxidation of some ferrous iron. However, it is interesting to note that the both the aqueous and ether phases at 36 h lie on the SFL (secondary fractionation line) and that the aqueous–ether fractionation has continued to increase slightly.

correspond to the models used for the ferric chloride complexes in Hill et al. (2009), so that the models could be used together to predict ferrous–ferric fractionation.

The UHF model is coupled with the 6-31G(d) basis set (Rassolov et al., 1998), and the hybrid DFT models, with basis sets 6-31G(d), 6-311G(d) (Frisch et al., 2004), and Ahlrich's VTZ (Schäfer et al., 1992). 6-31G(d) is a double split-valence basis set; 6-311G(d), a triple split-valence basis set; and Ahlrich's VTZ, a triple zeta basis set. The four models types are abbreviated: (1) UHF/6-31G(d); (2) B3LYP/6-31G(d); (3) B3LYP/6-311G(d); and (4) B3LYP/VTZ. The latter model uses Ahlrich's VTZ for Fe and Cl, and basis set 6-31G(d) for O and H. The models are calculated in vacuo, i.e., modeled with iron and its inner coordination sphere as gas phase molecules. Calculated vibrational frequencies are not scaled. Further details of the ferrous chloride ab initio models are given in Appendix A.

2.4.2. Speciation models of Fe–Cl complexes with varying chlorinity

Our speciation modeling of iron chloride complexes follows from earlier studies for Fe^{3+}–Cl–H_2O (e.g., Rabinowitch and Stockmayer, 1942; Bjerrum and Lukes, 1986; Bethke, 1996; Lee et al., 2003; Lee, 2004) and for Fe^{2+}–Cl–H_2O (e.g., Heinrich and Seward, 1990; Zhao and Pan, 2001; Lee, 2004; Liu et al., 2007). These models are used to determine the effects of the initial chloride to iron ratio, the acidity, and the ionic strength of the aqueous solution on the relative abundances of Fe–Cl species.

We calculated first-order relative abundances of each Fe–Cl complex at each chlorinity stoichiometrically using the activity model for HCl from Bromley (1973) (with interaction parameter "B" = 0.1433 for chloride—see Eq. (4a) and Table 1 in Bromley) and the appropriate equilibrium constants: (ferric chlorides: $C0 \Rightarrow C1$ (=30), $C1 \Rightarrow C2$ (=4.5), $C2 \Rightarrow C3$ (=0.15), $C3 \Rightarrow C4$ (=0.0078) from Bjerrum and Lukes (1986); ferrous chlorides: $D0 \Rightarrow D1$ (=0.347) and $D1 \Rightarrow D2$ (=0.038), calculated from Zhao and Pan (2001) and extrapolated to 20 °C. Activity coefficients for all other species were assumed to be unity.[6]

Calculations were iterated to determine final ionic strength and species concentrations. At each chlorinity, the amount of ferric iron remaining in the aqueous phase (after some dissolution into the ether phase) was used as the total ferric iron concentration. We assumed there was no oxidation of the ferrous complexes, since our control experiments showed no measurable oxidation of the ferrous complexes in the acid solution (pH < ~0) over the course of a day. No calculations for [Cl^-] < 0.3 M were performed, since this is the lowest chlorinity a solution of [$FeCl_2$] = 0.15 M would have.

Relative species concentrations were determined for an all-ferric solution, an all-ferrous solution, and a mixed 50:50 ferric–ferrous solution. In the mixed solution, the ferric species and ferrous species were treated independently except as each species contributed to the overall ionic

strength of the solution and, thus, to the activity of the chloride.

Similar stoichiometric calculations are described in more detail in Hill et al. (2009). However, as mentioned above (Section 2.2.1), the relative concentrations of the ferric chloride species in this work differ slightly from the previous work because the ionic strength in the current experiments is allowed to increase with chlorinity.

3. RESULTS

3.1. Extraction of ferric Fe from the aqueous phase into the ether phase

The amount of aqueous ferric iron dissolved into the ether as **C4** is strongly dependent on the chlorinity of the solution, climbing from less than 1% of the total ferric iron at 1.5 M Cl^- to a peak of >90% at [Cl^-] = 5.0 M. It is also dependent upon the amount of available ferric iron (Dodson et al., 1936). For a given chlorinity, the percentage of extracted Fe^{3+} decreases as the ferric/ferrous ratio decreases, lowering the available ferric iron as well as slightly lowering the effective chlorinity as chloride is increasingly utilized by the ferrous chloride complexes. Table 4 and Fig. A2 show the percentage of total ferric iron dissolved into the ether for each chlorinity and each different Fe^{2+}/$Fe_{total\ aq}$ initial ratio; Table 4 also shows the final Fe^{3+}/$Fe_{total\ aq}$ and Fe^{2+}/$Fe_{total\ aq}$ ratios for each experiment.

In the experiments shown in Fig. A2, both the acidity and the ionic strength increase with chlorinity. In Dodson et al.'s classic experiments there are always equal amounts of H^+ and Cl^- (as HCl); in our experiments there is slightly less H^+ than Cl^-, since there is additional chloride from the ferrous chloride (see Section 2.2.3); thus, slightly less **C4** is dissolved into the ether at each chlorinity than in Dodson et al.'s experiments. Apparently the amount of $FeCl_4^-$ dissolution depends on the availability of both H^+ and Cl^- (as well as Fe^{3+}) since the iron is most likely extracted as stoichiometric $HFeCl_4$ (i.e., $FeCl_4 \cdot H_3O \cdot nH_2O$). Compare with Fig. 4 in Hill et al. (2009).

Mass balance calculations of aqueous and ether iron concentration measurements are on average within 5% of the total initial calculated iron (comparable with the total uncertainty obtained by propagation of measurement error). This is similar to mass balance molarity measurements (within ~8%) by Nachtrieb and Conway (1948) and by Hill et al. (2009).

3.2. Ab initio models of Fe–Cl fractionation

Although there is some variation in the estimated β factors among the four sets of ab initio models, there are two prominent trends visible in the predicted Fe equilibrium isotope fractionation: (1) 1000 ln β is higher for each ferric chloride species than for the corresponding ferrous chloride species and (2) within the same oxidation state, 1000 ln β relative to **C0** or **D0** decreases with each Cl^- for OH_2 substitution (Table 2). Optimized geometries of the ferrous chloride complexes are shown in Fig. B1 in Appendix B in the Electronic Annex for B3LYP/6-31G(d). Reduced

---

[6] See Lee (2004) for a more rigorous treatment of speciation among mixed ferric and ferrous chloride solutions.
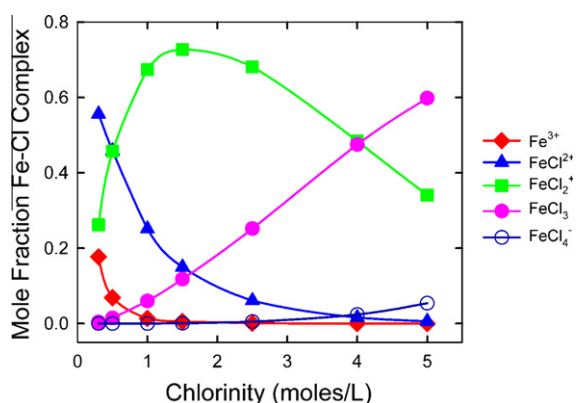
Fig. 1. Calculated fractional abundances of each ferric Fe–Cl complex, for varying chlorinities, relative to the total amount of ferric aqueous iron. Equilibrium constants are from Bjerrum and Lukes (1986), Cl activity model from Bromley (1973), ionic strength increases with Cl activity. [Fe^{3+}] at each chlorinity is the amount of aqueous ferric iron after extraction of some **C4** into the ether phase. See Table 3.
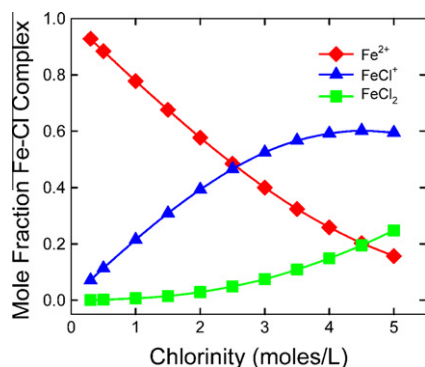

Fig. 2. Calculated fractional abundances of each ferrous Fe–Cl complex, for varying chlorinities, relative to the total amount of ferrous aqueous iron. Equilibrium constants are extrapolated from Zhao and Pan (2001), Cl activity model from Bromley (1973); ionic strength increases with Cl activity. [Fe^{2+}] = 0.15 M for all chlorinities. See Table 3.

partition function ratios for all models of the ferric and ferrous chloride species are shown in Fig. B2 in Appendix B.

3.3. Speciation models of Fe–Cl complexes with increasing chlorinity

The fractional abundances of aqueous iron chloride complexes relative to total aqueous iron depend on the

Table 3
Calculated fractional abundances of each Fe–Cl complex, for varying chlorinities, relative to the total amount of aqueous iron. Equilibrium constants for the ferric values are from Bjerrum and Lukes (1986); for the ferrous values, from Zhoa and Pan (2001). The activity model for chloride is from Bromley (1973); ionic strength increases with Cl activity. Activities for water and all Fe–Cl complexes are assumed to be 1. For ferric calculations [H$^+$] = [Cl$^-$] since all Fe^{3+} comes from powdered hematite. For ferrous calculations [H$^+$] = [Cl$^-$] − 2 ∗ [Fe^{2+}] since all Fe^{2+} comes from FeCl$_2$·4(H$_2$O) crystals. [Fe^{3+}] at each chlorinity is the amount of aqueous ferric iron after extraction of some **C4** into the ether phase. See text for details. See also Figs. 1 and 2.

[Fe$^{3+}_{aq}$]	Cl$^-$	C0	C1	C2	C3	C4
All-ferric aqueous solution with decreasing [Fe$^{3+}_{aq}$]						
0.150	0.3	0.177	0.556	0.262	0.004	0.000
0.150	0.5	0.069	0.458	0.457	0.015	0.000
0.150	1.0	0.014	0.251	0.674	0.060	0.000
0.148	1.5	0.005	0.150	0.727	0.118	0.001
0.138	2.5	0.001	0.061	0.681	0.252	0.005
0.076	4.0	0.000	0.016	0.484	0.475	0.024
0.014	5.0	0.000	0.006	0.341	0.598	0.054

Cl$^-$	D0	D1	D2
All-ferrous aqueous solution with [Fe^{2+}] = 0.15 M			
0.3	0.928	0.071	0.001
0.5	0.884	0.114	0.002
1.0	0.778	0.215	0.007
1.5	0.676	0.309	0.015
2.0	0.577	0.393	0.029
2.5	0.485	0.466	0.049
3.0	0.400	0.525	0.075
3.5	0.324	0.567	0.109
4.0	0.259	0.592	0.149
4.5	0.203	0.602	0.195
5.0	0.157	0.595	0.248

amounts of chloride and iron, the acidity, and the ionic strength of the aqueous solution. In general, complexes with higher Cl/Fe ratios become more abundant as the chloride activity increases (Table 3 and Figs. 1, 2). The total iron used in the ferric chloride speciation calculations is the [Fe$^{3+}_{aq}$] remaining after dissolution of some **C4** into the ether phase. **C2** is the most abundant complex between 0.5 and 4 M chlorinity. **C3** increases in abundance with rising [Cl$^-$], overtaking **C2** > 4 M, while **C1** decreases steadily. **C4** abundances are initially low but increase gradually. The decrease in total ferric iron with increasing chlorinity results in a slight boost in species with higher Cl/Fe (e.g., for [Cl$^-$] = 5 M and [Fe^{3+}] = 0.014 M, **C3** and **C4** increase

Table 2
Reduced partition function ratios (shown as 1000 ln β) for all models of each Fe–Cl complex used in these experiments in per mil (‰). Values for the ferric chloride complexes are taken from Hill and Schauble (2008). The ferrous chloride complexes were developed for this work. The vibrational frequencies used in these calculations are unscaled.

	Ferric					Ferrous			1000 ln α (**C0–D0**)
	C0	C1	C2	C3	C4	D0	D1	D2	
B3LYP/6-311G(d)	9.41	8.54	8.10	7.13	7.17	6.39	5.98	5.91	3.02
B3LYP/6-31G(d)	8.93	8.04	7.61	7.05	7.46	5.68	5.35	4.86	3.25
B3LYP/VTZ	9.59	8.57	8.13	7.13	7.14	6.57	6.06	5.76	3.02
UHF/6-31G(d)	9.73	9.12	8.73	7.74	8.25	5.42	5.34	5.08	4.31

$\sim$2% and $\sim$1%, respectively, while **C2** decreases, compared to abundances for which $[Cl^-] = 5$ M and $[Fe^{3+}] = 0.15$ M).

In the ferrous chloride speciation models, the total iron is $[Fe^{2+}] = 0.15$ M for all chlorinities. An initially high **D0** decreases steadily with rising chlorinity being overtaken by a rising **D1** at $[Cl^-] > 2.5$ M. **D2** increases more slowly with rising chlorinity. Computational details for both sets of speciation modeling are given in Section 2.4.2.

One effect of having ferric and ferrous species together in the solution is to lower the effective chloride concentration slightly (since some chloride is taken up by all Fe–Cl species). Modeling of a half ferric–half ferrous solution shows very similar speciation to an all-ferric solution and an all-ferrous solution at the same chlorinities. Note that for a given chlorinity, the most abundant Fe^{3+} species has a higher Cl/Fe ratio than the dominant Fe^{2+} species.

When the speciation models of this work are compared with the speciation modeling of the ferric chlorides in Hill et al. (2009), we see that the constant high ionic strength ($\sim$5) in Hill et al. results in increased chloride activity at lower chorinities. This results in higher abundances of complexes with higher Cl/Fe ratios at smaller chlorinities than when ionic strength increases with chlorinity as in this work.

3.4. Experimental fractionations between aqueous and ether phases ($\Delta^{56}Fe_{(aq–eth)}$)

As the chlorinity increases, the measured fractionation between the aqueous and the ether phases ($\Delta^{56}Fe_{(aq–eth)}$) in all-ferric solutions decreases by 0.93‰ (from 0.73‰ at $[Cl^-] = 1.5$ M to -0.19‰ at $[Cl^-] = 5.0$ M), as expected quantitatively from Hill et al. (2009). Among the experiments at a given chlorinity, $\Delta^{56}Fe_{(aq–eth)}$ decreases as the percentage of aqueous ferrous iron increases (Table 5 and Fig. 3).

The calculated fractionation between the aqueous and the ether phases $\Delta^{56}Fe_{(aq–eth)}$ for the all-ferrous solutions varies only slightly (<0.12‰) with the same change in chlorinity (Table 6 and Fig. 3). The aqueous and ether $\delta^{56}Fe$ and $\delta^{57}Fe$ values for each experiment all plot along the terrestrial mass fractionation line (TFL), demonstrating mass-dependent isotopic fractionation and the lack of interference from ^{54}Cr in the MC-ICP-MS (Fig. A3).

3.5. Experimental fractionations between ferric and ferrous chloride species ($1000 \ln \alpha$ ($Fe^{3+}–Fe^{2+}$))

There is an overall decrease in the fractionation between the ferric species and the ferrous species ($1000 \ln \alpha$ ($Fe^{3+}–Fe^{2+}$)) with increasing chlorinity, from 3.4‰ for $[Cl^-] = 1.5$ M to 2.4‰ for $[Cl^-] = 5.0$ M (Table 6 and Fig. 4).

3.6. Theoretical predictions for ferric–ferrous fractionation from the ab initio models ($\Delta^{56}Fe_{(aq–eth)}$ and $1000 \ln \alpha$ ($Fe^{3+}–Fe^{2+}$))

Predictions of all-ferric $\Delta^{56}Fe_{aq–eth}$ and the all-ferrous $\Delta^{56}Fe_{aq–eth}$ from ab initio models and speciation models for each experiment at each chlorinity are calculated as

$$\Delta^{56}Fe_{aq–eth} = \{A\}\left\{\sum_i (1000 \ln \beta_{Ci})(X_{Ci\,aq})\right\} + \{B\}$$
$$\times \left\{\sum_i (1000 \ln \beta_{Di})(X_{Di\,aq})\right\}$$
$$- 1000 \ln \beta_{FeCl_4^-} \qquad (5)$$

where $A = \frac{[\text{total aqueous ferric iron}]}{[\text{total aqueous iron}]}$ and $B = \frac{[\text{total ferrous iron}]}{[\text{total aqueous iron}]}$ and X_{Di} is the fraction of ferrous complex **D***i* to the total ferrous iron in the aqueous solution and X_{Ci} is the final fraction of ferric complex **C***i* to the total ferric iron in the aqueous solution (after dissolution of some **C4** into the ether) (see Section 2.2.8). Once the final system is at equilibrium, we assume there is no fractionation between the aqueous **C4** and the dissolved ethereal **C4** since both instances of **C4** have the same inner sphere bond environment (i.e., oxidation state, coordination number, and bond partners) and any kinetic processes involved in dissolution will also have come to equilibrium. Predictions of $1000 \ln \alpha$ ($Fe^{3+}–Fe^{2+}$) are then calculated from Eq. (4).

The predictions and the experimental data for $1000 \ln \alpha$ ($Fe^{3+}–Fe^{2+}$) vs. chlorinity (Table 7 and Fig. 5) all show a downward trend with increasing chlorinity, although the theoretical models have shallower slopes. The three DFT models predict smaller ferric–ferrous fractionations in general than shown by the experimental data, while the UHF/6-31G(d) model predictions are slightly larger than the experimental data for $[Cl] \geqslant 2$ M.

The predicted and the experimental values of the all-ferric $\Delta^{56}Fe_{aq–eth}$ also follow similar downward trends (Fig. 6A). The experimental data are smaller than predicted values from models B3LYP/6-311G(d) and B3LYP/VTZ but larger than predictions from the two other models (as in Hill et al., 2009). The predicted values of the all-ferrous $\Delta^{56}Fe_{aq–eth}$ have much more shallow downward slopes than the all-ferric predictions (Fig. 6B). The three DFT ferrous models all predict higher fractionation values than the experimental data, while the UHF model predictions are smaller than the data.

3.7. Reversal experiment

Isotopic equilibrium within 60 min is inferred from the three criteria detailed in Section 2.3. First, each phase moves along a distinct linear mixing line toward the secondary fractionation line (SFL) in three-isotope space as time progresses (Fig. 7 and Table 8). Second, the aqueous and ether mixing lines intersect the SFL at $\delta^{56}Fe = -7.6 \pm 0.03$‰ and -6.6 ± 0.02‰, respectively, resulting in $\Delta^{56}Fe_{aq–eth} = -1.0 \pm 0.04$‰, compared to -0.83 ± 0.02‰ of the forward experiment. $\Delta^{56}Fe_{aq–eth}$ has changed from 58.3‰ at $t = 0$ min to -0.2‰ at $t = 60$ min, which is 99%[7] of the way to an estimated equilibrium value of 1.0‰. In an unspiked forward experiment, the change in

---

[7] We define the % equilibrium value of $X = 100 \ (X_{\text{at 60 min}} - X_{\text{at 0 min}})/(X_{\text{SFL intersection point}} - X_{\text{at 0 min}})$ where X is $\delta^{56}Fe_{aq}$, $\delta^{56}Fe_{eth}$, or $\Delta^{56}Fe_{aq–eth}$. Aq: $(-7.3 - (0.7))/8.3 = 0.96$; eth: $(-57.6 - (-7.2))/51.0 = 0.99$; $\Delta^{56}Fe_{aq–eth}$: $(58.3 - (-0.2))/(58.3 - (-1.0)) = 0.99$.
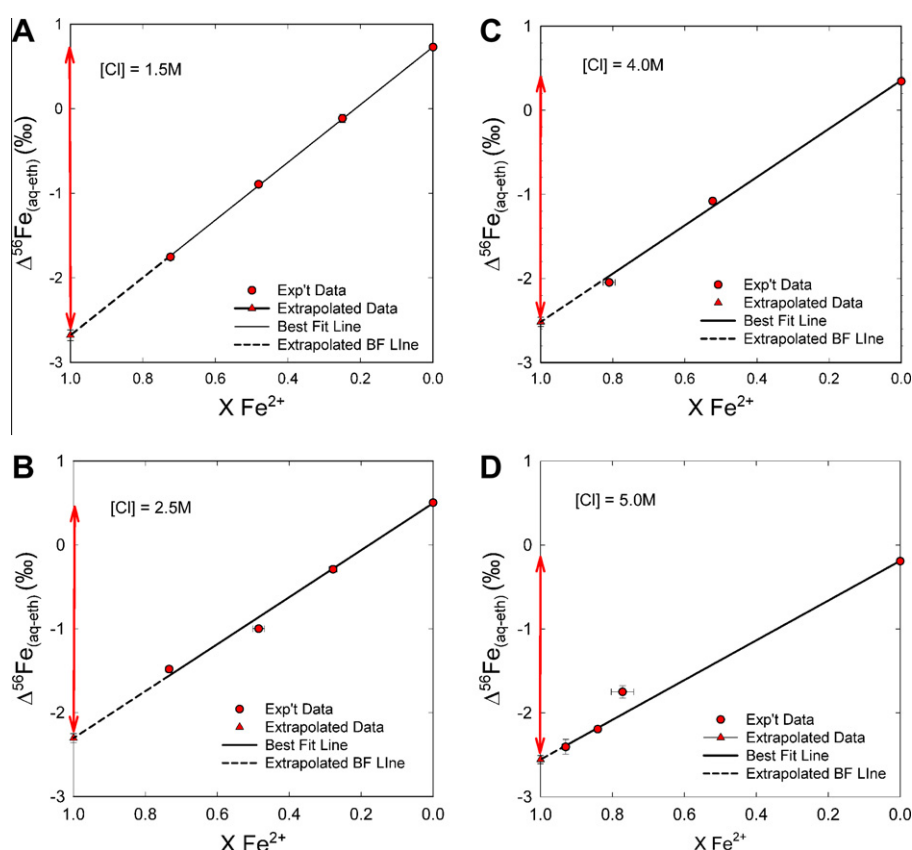
Fig. 3. Fractionation between the ferric chloride species and the ferrous chloride species for experiments at chlorinities of 1.5 M (top left), 2.5 M (bottom left), 4.0 M (top right), and 5.0 M (bottom right). Each (gray/red) circle represents a separate experimental $\Delta^{56}Fe_{aq-eth}$ for a given chlorinity and given Fe^{2+}/Fe_{total} ratio. The solid line in each graph is the best-fit line for the data points, calculated using a modified York regression, extrapolated (dotted line) to determine $\Delta^{56}Fe_{aq-eth}$ ($Fe^{2+}/Fe_{total} = 1$). The vertical red arrow on the ordinate axis is the graphic representation of $1000 \ln \alpha$ ($Fe^{3+}-Fe^{2+}$). $1000 \ln \alpha$ ($Fe^{3+}-Fe^{2+}$) is calculated as $\Delta^{56}Fe_{aq-eth}$ ($Fe^{2+}/Fe_{total} = 0$) $- \Delta^{56}Fe_{aq-eth}$ ($Fe^{2+}/Fe_{total} = 1$). The three leftmost data points for the bottom right graph (Cl = 5.0 M) are closer together because much more Fe^{3+} has been extracted into the ether due to higher chlorinity, leaving a larger final aqueous Fe^{2+}/Fe_{total}. Error bars are standard error one sigma. See Tables 4–6 and Fig. A2. (For interpretation of the references to color in this figure legend, the reader is referred to the web version of this article.)
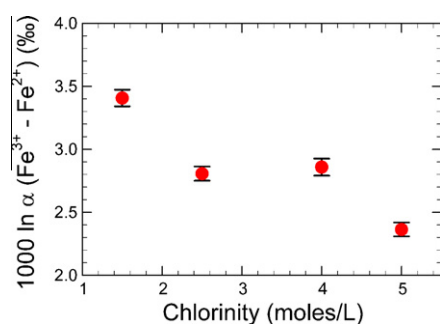

Fig. 4. Experimental data for the ferric–ferrous fractionation $1000 \ln \alpha$ ($Fe^{3+}-Fe^{2+}$) vs. chlorinity. Each red circle is the calculated result of three or four different experiments. Error bars are standard error one sigma. See Table 6. (For interpretation of the references to color in this figure legend, the reader is referred to the web version of this article.)

$\Delta^{56}Fe_{aq-eth}$ over 60 min is less than 2.5‰; thus, 99% equilibration is not expected to be analytically distinguishable from 100%, given measurement uncertainties.

Third, the $^{56}Fe/^{54}Fe$ per mil composition of the aqueous phase must change by 8.3‰ ($= 0.7 - (-7.6)$) along the $\delta^{56}Fe$ axis while the ether phase must change by 51.0‰ ($=-57.6 - (-6.6)$). At time = 60 min, the aqueous phase has moved 96%[7] and the ether phase 99%[7] of the way along their respective mixing lines toward their final values on the SFL. The bulk isotopic composition, calculated from Fe concentration and isotope values at 60 min, is located at $\delta^{57}Fe = -7.0 \pm 0.03‰$ and $\delta^{56}Fe = -7.3 \pm 0.015‰$. See Section 4.5 for a discussion of these results.

4. DISCUSSION

4.1. General trends in ab initio fractionation factors

The most significant feature of all the ab initio models is the nearly linear decrease in $1000 \ln \beta$ of the ferric species relative to C0 and of the ferrous species relative to D0 as Cl^- is progressively substituted for OH_2 in the inner coordination sphere (Table 2). All of the ferrous species have smaller $1000 \ln \beta$ than do their ferric counterparts,

P.S. Hill et al. / Geochimica et Cosmochimica Acta 74 (2010) 6669–6689

Table 4
Division of total iron between aqueous and ether phases for different chlorinities. Each concentration was measured independently at least three times. Reported errors are one standard error. Units are mole/l. Total Fe is the calculated concentration of the original iron solution before the addition of ether. Fe_{aq}, Fe_{eth}, and $Fe_{total aq}$ are measured quantities. Fe_{aq} errors result from measurement with an auto-pipette while Fe_{eth} errors contain measurement errors from a disposable pipette, an auto-pipette, and a 10 ml graduated cylinder. Final fractions of Fe^{3+} and Fe^{2+} in the aqueous solution are calculated from measured values (see Section 3.1 and Fig. A2).

Exp.	Cl⁻	Calculated values			Measured values			Calculated from measured values				
		Initial total Fe	Initial Fe^{2+}/$Fe_{total aq}$	Initial Fe^{3+}/$Fe_{total aq}$	Fe^{3+}_{eth}	Fe^{2+}_{aq}	$Fe_{total aq}$	Fe^{3+}_{aq} [a]	% Fe^{3+}_{eth}/total Fe^{3+} [b]	Final Fe^{3+}/$Fe_{total aq}$	Final Fe^{2+}/$Fe_{total aq}$	$Fe_{tot\ aq+eth}$ [c]
RD40	1.5	0.15	0.00	1.00	$0.000038 \pm 8.8E{-}08$	0.0000 ± 0.0	$0.1482 \pm 1.3E{-}03$	0.1482	0.026	1.000	0.000 ± 0.0000	0.148
RD41	1.5	0.15	0.25	0.75	$0.000027 \pm 1.9E{-}07$	$0.0356 \pm 1.6E{-}04$	$0.1423 \pm 1.7E{-}03$	0.1067	0.025	0.750	0.250 ± 0.0032	0.142
RD42	1.5	0.15	0.50	0.50	$0.000022 \pm 3.6E{-}07$	$0.0757 \pm 1.3E{-}03$	$0.1575 \pm 2.4E{-}04$	0.0818	0.027	0.519	0.481 ± 0.0083	0.158
RD43	1.5	0.15	0.75	0.25	$0.000011 \pm 3.3E{-}07$	$0.1105 \pm 1.1E{-}03$	$0.1526 \pm 1.3E{-}03$	0.0421	0.027	0.276	0.724 ± 0.0095	0.153
RD50	2.5	0.15	0.00	1.00	$0.000899 \pm 3.6E{-}06$	0.0000 ± 0.0	$0.1382 \pm 6.9E{-}04$	0.1382	0.646	1.000	0.000 ± 0.0000	0.139
RD51	2.5	0.15	0.25	0.75	$0.000750 \pm 4.2E{-}06$	$0.0367 \pm 1.2E{-}03$	$0.1321 \pm 2.6E{-}03$	0.0954	0.780	0.722	0.278 ± 0.0106	0.133
RD52	2.5	0.15	0.50	0.50	$0.000555 \pm 4.2E{-}06$	$0.0697 \pm 2.3E{-}03$	$0.1438 \pm 3.1E{-}04$	0.0741	0.743	0.515	0.485 ± 0.0160	0.144
RD53	2.5	0.15	0.75	0.25	$0.000297 \pm 2.3E{-}07$	$0.1018 \pm 1.0E{-}03$	$0.1387 \pm 1.1E{-}03$	0.0369	0.799	0.266	0.734 ± 0.0093	0.139
RD60	4.0	0.15	0.00	1.00	$0.07880 \pm 4.1E{-}04$	0.0000 ± 0.0	$0.0764 \pm 6.4E{-}04$	0.0764	50.783	1.000	0.000 ± 0.0000	0.155
RD61	4.0	0.15	0.35	0.65	$0.04880 \pm 3.4E{-}05$	$0.0516 \pm 0.0E{+}00$	$0.0986 \pm 1.6E{-}04$	0.0470	50.939	0.477	0.523 ± 0.0008	0.147
RD62	4.0	0.15	0.75	0.25	$0.01697 \pm 3.4E{-}05$	$0.1149 \pm 1.6E{-}03$	$0.1418 \pm 2.2E{-}03$	0.0269	38.682	0.190	0.810 ± 0.0169	0.159
RD70	5.0	0.15	0.00	1.00	$0.1494 \pm 2.2E{-}03$	0.0000 ± 0.0	$0.0138 \pm 2.3E{-}05$	0.0138	91.542	1.000	0.000 ± 0.0000	0.163
RD71	5.0	0.15	0.25	0.75	$0.1178 \pm 5.2E{-}04$	$0.0290 \pm 1.1E{-}03$	$0.0376 \pm 5.4E{-}04$	0.0086	93.227	0.228	0.772 ± 0.0313	0.155
RD72	5.0	0.15	0.50	0.50	$0.0755 \pm 1.1E{-}03$	$0.0630 \pm 2.8E{-}04$	$0.0749 \pm 5.5E{-}04$	0.0119	86.393	0.159	0.841 ± 0.0072	0.150
RD73	5.0	0.15	0.75	0.25	$0.0428 \pm 5.3E{-}04$	$0.0975 \pm 1.2E{-}03$	$0.1048 \pm 1.1E{-}03$	0.0073	85.384	0.070	0.930 ± 0.0098	0.148

[a] $Fe^{3+}_{aq} = Fe_{total aq} - Fe^{2+}_{aq}$.
[b] % Fe^{3+}_{eth}/total $Fe^{3+} = 100 * Fe^{3+}_{eth}/(Fe^{3+}_{eth} + Fe^{3+}_{aq})$.
[c] $Fe_{tot\ aq+eth} = Fe_{total aq} + Fe^{3+}_{eth}$.

Table 5
Experimental values of Δ^{56}Fe$_{(aq–eth)}$ for each chlorinity and final Fe^{2+}/Fe$_{total\ aq}$ (see Fig. 3). Uncertainties are one standard error.

Exp.	Cl$^-$ (M)	Final meas.					
		Fe^{2+}/Fe$_{total\ aq}$[a]	Δ^{56}Fe$_{aq–eth}$ (‰)	δ^{56}Fe$_{aq}$ (‰)	δ^{57}Fe$_{aq}$ (‰)	δ^{56}Fe$_{eth}$ (‰)	δ^{57}Fe$_{eth}$ (‰)
RD40	1.5	0.000 ± 0.000	0.728 ± 0.020	0.126 ± 0.017	0.155 ± 0.030	-0.602 ± 0.010	-0.879 ± 0.004
RD41	1.5	0.250 ± 0.003	-0.115 ± 0.048	0.213 ± 0.019	0.341 ± 0.031	0.328 ± 0.044	0.472 ± 0.044
RD42	1.5	0.481 ± 0.008	-0.894 ± 0.032	0.305 ± 0.017	0.459 ± 0.021	1.198 ± 0.027	1.752 ± 0.036
RD43	1.5	0.724 ± 0.010	-1.753 ± 0.035	0.470 ± 0.024	0.655 ± 0.036	2.224 ± 0.025	3.280 ± 0.036
RD50	2.5	0.000 ± 0.000	0.503 ± 0.015	0.217 ± 0.005	0.320 ± 0.013	-0.286 ± 0.034	-0.429 ± 0.022
RD51	2.5	0.278 ± 0.011	-0.291 ± 0.016	0.310 ± 0.013	0.487 ± 0.021	0.601 ± 0.010	0.861 ± 0.020
RD52	2.5	0.485 ± 0.016	-0.999 ± 0.021	0.435 ± 0.015	0.653 ± 0.030	1.434 ± 0.0146	2.083 ± 0.0382
RD53	2.5	0.734 ± 0.009	-1.481 ± 0.032	0.784 ± 0.028	1.047 ± 0.020	2.264 ± 0.024	3.342 ± 0.042
RD60	4.0	0.000 ± 0.000	0.344 ± 0.025	0.385 ± 0.022	0.562 ± 0.024	0.041 ± 0.012	0.062 ± 0.013
RD61	4.0	0.523 ± 0.001	-1.079 ± 0.038	0.040 ± 0.016	0.086 ± 0.017	1.119 ± 0.034	1.629 ± 0.052
RD62	4.0	0.810 ± 0.017	-2.046 ± 0.014	0.350 ± 0.014	$0.5160.022$	2.397 ± 0.004	3.566 ± 0.029
RD70	5.0	0.000 ± 0.000	-0.193 ± 0.028	0.203 ± 0.025	0.297 ± 0.057	0.396 ± 0.012	0.581 ± 0.015
RD71	5.0	0.772 ± 0.031	-1.750 ± 0.073	-0.854 ± 0.071	-1.301 ± 0.105	0.896 ± 0.017	1.340 ± 0.030
RD72	5.0	0.841 ± 0.007	-2.194 ± 0.020	-0.567 ± 0.014	-0.841 ± 0.025	1.627 ± 0.015	2.377 ± 0.035
RD73	5.0	0.930 ± 0.010	-2.405 ± 0.089	-0.059 ± 0.080	-0.036 ± 0.104	2.346 ± 0.039	3.492 ± 0.055

[a] This column is taken from Table 4.

Table 6
Experimental values of 1000 ln α (Fe^{3+}–Fe^{2+}) for each chlorinity. Uncertainties are one standard error. See Fig. 4.

Cl (M)	Δ^{56}Fe$_{(aq–eth)}$ for Fe^{2+}/Fe$_{total}$ = 0[a]	Δ^{56}Fe$_{(aq–eth)}$ for Fe^{2+}/Fe$_{total}$ = 1	1000 ln α (Fe^{3+}–Fe^{2+})	Best-fit line (see Fig. 3)	
				Slope	Intercept
1.5	0.728 ± 0.020	-2.679 ± 0.063	3.407 ± 0.066	-3.409 ± 0.061	0.730 ± 0.016
2.5	0.503 ± 0.015	-2.304 ± 0.054	2.807 ± 0.056	-2.802 ± 0.053	0.498 ± 0.013
4	0.344 ± 0.025	-2.515 ± 0.064	2.859 ± 0.068	-2.871 ± 0.060	0.356 ± 0.019
5	-0.193 ± 0.028	-2.556 ± 0.048	2.364 ± 0.055	-2.367 ± 0.044	-0.189 ± 0.019

[a] This column is taken from Table 5.

consistent with theoretical predictions that the heavier isotope prefers the higher oxidation state (e.g., Schauble, 2004).

Also significant is the smaller rate of decrease of 1000 ln β of the ferrous chloride species with increasing Cl/Fe compared to the rate of decrease of the ferric chloride species. The slopes of the best-fit trendlines for the octahedral ferric complexes (**C0–C3**) range from −0.61 to −0.78 (‰/Fe–Cl bond) compared to best-fit slopes of −0.17 to −0.41 (‰/Fe–Cl bond) for the octahedral ferrous species (**D0–D2**) (**C4** has a slightly higher β due to its smaller coordination number of four). This implies that nonredox changes in the ferric speciation are more significant to the overall fractionation signal than comparable changes in ferrous speciation. This can be easily seen in Fig. 8, which shows the predicted isotopic fractionation 1000 ln α between **C4** and each of the other iron species for the B3LYP/6-311G(d) model (calculated from Table 2).

The decrease in fractionation with increasing [Cl$^-$] is significant for two reasons: (1) it shows that redox fractionation is sensitive to nonredox properties of the solution and (2) it suggests that other ligands present in an aqueous iron environment are potentially important drivers of frac-

tionation between iron-bearing species and should also be considered when interpreting iron isotope fractionations in geological records.

4.2. Effects of solution chemistry on ferrous/ferric fractionation

The reduction in ferric–ferrous fractionation with increasing chlorinity is most simply explained by the changes in aqueous solution chemistry. As the chlorinity rises, species with higher Cl/Fe ratios and lower 1000 ln βs become more common (Figs. 1 and 2). Although 1000 ln β decreases for both ferric and ferrous species with ever larger Cl/Fe ratios, the decrease is more rapid for the ferric species (Section 4.1 and Fig. 8); also, at a given [Cl$^-$] the dominant ferric species has a higher Cl/Fe ratio than the dominant ferrous species. Both these factors result in an overall decline in the ferric–ferrous fractionation and thus in the redox isotopic signature as chlorinity rises. This is shown in the experimental data by comparing the change in the all-ferric fractionation, Δ^{56}Fe$_{aq–eth}$ (Fe^{2+}/Fe$_{total}$ = 0), to the change in the all-ferrous fractionation, Δ^{56}Fe$_{aq–eth}$ (Fe^{2+}/Fe$_{total}$ = 1), of the aqueous phase relative to the **C4**-ether phase. The ferric

Table 7
Theoretical predictions of $\Delta^{56}Fe_{aq-eth}$ ($Fe^{2+}/Fe_{total} = 0$), $\Delta^{56}Fe_{aq-eth}$ ($Fe^{2+}/Fe_{total} = 1$), and $1000 \ln \alpha$ ($Fe^{3+}-Fe^{2+}$) in ‰ for increasing chlorinity for each ab initio model. $1000 \ln \alpha$ ($Fe^{3+}-Fe^{2+}$) is the predicted $\Delta^{56}Fe_{aq-eth}$ ($Fe^{2+}/Fe_{total} = 0$) − $\Delta^{56}Fe_{aq-eth}$ ($Fe^{2+}/Fe_{total} = 1$). See Figs. 5 and 6.

$[Fe^{3+}_{aq}]$	Cl	$\Delta^{56}Fe_{aq-eth}$ ($Fe^{2+}/Fe_{total} = 0$)	$\Delta^{56}Fe_{aq-eth}$ ($Fe^{2+}/Fe_{total} = 1$)	$1000 \ln \alpha$ ($Fe^{3+}-Fe^{2+}$)	$\Delta^{56}Fe_{aq-eth}$ ($Fe^{2+}/Fe_{total} = 0$)	$\Delta^{56}Fe_{aq-eth}$ ($Fe^{2+}/Fe_{total} = 1$)	$1000 \ln \alpha$ ($Fe^{3+}-Fe^{2+}$)
		UHF/6-31G(d)			*B3LYP/6-31G(d)*		
0.150	0.3	0.861	−2.836	3.70	0.613	−1.804	2.42
0.150	0.5	0.704	−2.840	3.54	0.422	−1.819	2.24
0.150	1.0	0.524	−2.849	3.37	0.235	−1.856	2.09
0.148	1.5	0.435	−2.860	3.29	0.162	−1.895	2.06
0.138	2.5	0.253	−2.871	3.12	0.036	−1.934	1.97
0.076	4.0	−0.004	−2.884	2.88	−0.120	−1.974	1.85
0.014	5.0	−0.144	−2.898	2.75	−0.198	−2.015	1.82
		B3LYP/6-311G(d)			*B3LYP/BVTZ*		
0.150	0.3	1.395	−0.809	2.20	1.481	−0.607	2.09
0.150	0.5	1.199	−0.828	2.03	1.269	−0.630	1.90
0.150	1.0	0.992	−0.871	1.86	1.053	−0.685	1.74
0.148	1.5	0.895	−0.914	1.81	0.952	−0.740	1.69
0.138	2.5	0.709	−0.955	1.66	0.761	−0.794	1.56
0.076	4.0	0.446	−0.995	1.44	0.490	−0.848	1.34
0.014	5.0	0.294	−1.031	1.33	0.333	−0.899	1.23

fractionation relative to **C4** decreases by 0.92‰ (from 0.73‰ to −0.19‰) from 1.5 M to 5.0 M [Cl⁻], while the ferrous fractionation relative to **C4** shows a very small increase of 0.12‰ (−2.68‰ to −2.56‰) in the same range (Table 6 and Fig. 6). This causes an overall decrease in the ferric–ferrous fractionation, $1000 \ln \alpha$ ($Fe^{3+}-Fe^{2+}$), of ∼1.04‰ (3.41–2.36‰) for $[Cl^-] = 1.5$ M to 5.0 M, or an average of 0.3‰/M [Cl⁻] in this chlorinity range.

The ionic strength of the aqueous solution also influences the redox fractionation by its effect on speciation shifts. This can be seen by comparing changes in the all-ferric $\Delta^{56}Fe_{aq-eth}$ in the current work to $\Delta^{56}Fe_{aq-eth}$ changes in the all-ferric experiments in Hill et al. (2009) (see Section 2.2.1). In the current experiments, ionic strength (and consequently the chloride activity coefficient) rises with chlorinity, while in the Hill et al. (2009) experiments the ionic strength remains relatively constant (∼5), resulting in a smaller overall change in chloride activity, greater abundance of high Cl/Fe complexes at a given $[Cl^-] < 5$ M and lower aqueous–ether fractionation. The change in the all-ferric $\Delta^{56}Fe_{aq-eth}$ from the current study is about twice as large as $\Delta^{56}Fe_{aq-eth}$ of Hill et al. (2009) for $[Cl^-] = 1.5$–5.0 M.

Our theoretical predictions of $1000 \ln \alpha$ ($Fe^{3+}-Fe^{2+}$) indicate a gradual decrease with increasing chlorinity at about half the observed rate: (0.51, 0.49, 0.46, and 0.24‰ vs. 1.04‰ for chlorinities between 1.5 and 5 M) (Fig. 5 and Tables 6, 7). This is puzzling, especially since theoretical predictions of all-ferric $\Delta^{56}Fe_{aq-eth}$ in Hill et al. (2009) are quite close to the experimental values (within ∼0.2‰). A closer look shows that ferrous $\Delta^{56}Fe_{aq-eth}$ are in poorer agreement with observations (Tables 6, 7 and Fig. 6).

The theoretical models predict the largest ferric–ferrous fractionations at the lowest chlorinities. At $[Cl^-] = 0$, $1000 \ln \alpha$ ($Fe^{3+}-Fe^{2+}$) = $1000 \ln \beta$ (**C0**) − $1000 \ln \beta$ (**D0**); predictions range from 3.0‰ to 4.2‰, depending on the model (Table 2 and Fig. 5). The large fractionation at low (or no) chlorinity is a direct result of the greatest abundance

of complexes with smaller Cl/Fe ratios and higher $1000 \ln \beta$s (Fig. 8). This is demonstrated in the application of our theoretical predictions to the redox experiments of Johnson et al. (2002) and Welch et al. (2003), discussed in Appendix A.1.4. The ab initio models predict decreases in $1000 \ln \beta$ of ∼0.3–0.5‰ (depending on the model) as chlorinity increases from 0 to 111 mM, which are not seen in the experiments.

In sum, the redox fractionation signature of Fe in solution is influenced by the following: (1) the oxidation states of the species in solution; (2) the relative abundances of complexes present in the solution; and (3) the fractionation between the specific complexes present in the solution. The ionic strength of the overall solution also influences the fractionation, acting through its effect on the activity of the ions. The experimentally determined decrease in the redox isotope signal due to increasing chlorinity averages to 0.3‰/M [Cl⁻][8] in the range $1.5 M \leqslant [Cl^-] \leqslant 5$ M while the theoretical predictions are 0.13‰, 0.09‰, 0.07‰, and 0.01‰/M [Cl⁻] (calculated from Table 7). At smaller chlorinities the theoretical models predict a larger redox fractionation. Thus, for iron chloride in solution, the oxidation state of a species is the main contributor to the isotope signal, but speciation in aqueous solution or at a fluid/mineral boundary may significantly modify the redox fractionation or even impart a signature absent from any redox partitioning.

4.3. Potential sources of error

The experimental results are subject to measurement errors. The measurement of $Fe^{2+}/Fe_{total\,aq}$ is critical to the calculation of the redox fractionation (Section 2.2.8). The York regression accounts for uncertainties in $Fe^{2+}/Fe_{total\,aq}$
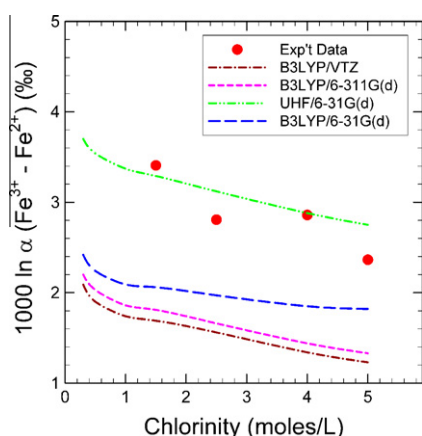
---

[8] $(3.407 − 2.364)‰/(1.5 − 5.0)$ M $= −0.30‰$/M [Cl⁻].

Fig. 5. Comparison of ab initio model predictions and experimental data for the ferric–ferrous fractionation $1000 \ln \alpha$ $(Fe^{3+}–Fe^{2+})$ vs. chlorinity. Compare with Tables 6 and 7.

as well as in isotopic ratios. Uncertainties in measured iron concentrations in the aqueous solution were propagated through all other calculations, namely, the calculation of the all-ferrous $\Delta^{56}Fe_{aq-eth}$ and consequently $1000 \ln \alpha$ $(Fe^{3+}–Fe^{2+})$. Possible errors due to the experimental setup are discussed in detail in Hill et al. (2009).

Errors in the theoretical predictions possibly come from two sources: calculated vibrational frequencies (discussed in more detail in Appendix A and in Hill and Schauble, 2008) and speciation modeling. The equilibrium constants and the chloride activity model used in the ferric chloride speciation models (Section 2.4.2) are well established in the literature, and the theoretical predictions of the all-ferric $\Delta^{56}Fe_{aq-eth}$ for this work (Fig. 6A) are very similar to those shown in Fig. 8 in Hill et al. (2009), despite the differences in speciation. The ferrous chloride speciation models seem to be less well established; we chose the equilibrium constants we felt were best supported by experimental data in the literature, and then extrapolated to the temperature we needed (see Section 2.4.2). The overestimation of the all-ferrous

$\Delta^{56}Fe_{aq-eth}$ by the three DFT ab initio models is reflected in the underestimation of $1000 \ln \alpha$ $(Fe^{3+}–Fe^{2+})$ by these models. The large range in the ferrous predictions is puzzling. It is also interesting that the best theoretical prediction is from the less-rigorous UHF model, perhaps due to a cancellation of errors.

4.4. C4-ether spectator phase

The use of diethyl ether to extract exchangeable $FeCl_4^-$ in these experiments makes it possible to monitor isotopic fractionation behavior of the aqueous solution under varying chemistries (in this case, different chlorinities). Since the aqueous phase can equilibrate with the spectator phase, aliquots of either phase may easily be removed for measurement without disturbing fractionations between system components. The existence of two phases in the system also makes it possible to perform reversal experiments. This two-phase experimental design should also have applications to a wider range of isotope fractionation experiments.

4.5. Redox reversal experiment

Considered numerically in terms of the distance each phase must travel along the $\delta^{56}Fe$ axis in three-isotope space, the ether phase of the redox reversal experiment, is at 98% of equilibration after 20 min and at 99% at 60 min. The aqueous phase is at 96% of equilibration after 40–60 min. As described in Section 2.3, each phase moves along a mixing line that intersects the SFL. The final equilibrated $\Delta^{56}Fe_{aq-eth}$ will be the difference in $\delta^{56}Fe$ of these two intersection points in three-isotope space. This distance for the reversal experiment is $-1.0‰$ compared to the $-0.83‰$ of the forward experiment. For an unspiked experiment, in which the $\delta^{56}Fe$ change in both phases is considerably less than 2‰, 99% equilibration is unlikely to be resolvable from 100% equilibration.

The aqueous phase equilibrates more slowly than the ether phase; this is most likely due to incomplete mixing. The ether occupies a flat disk-shaped space near the top
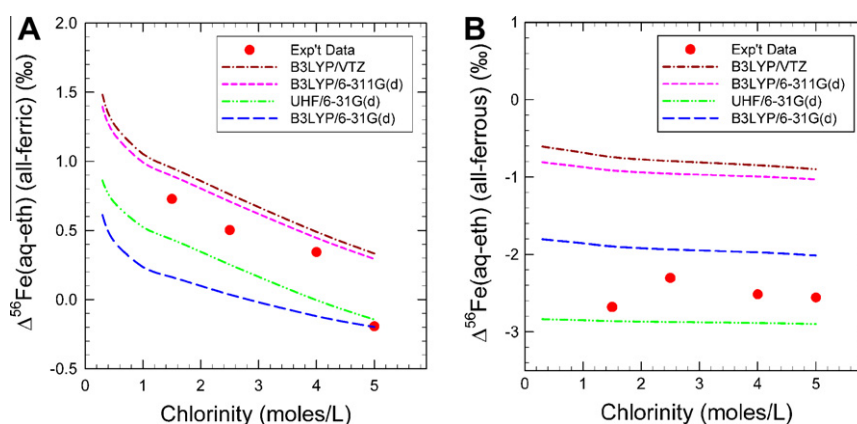

Fig. 6. Theoretical predictions of aqueous–ether fractionation of an all-ferric chloride solution (A) and an all-ferrous chloride solution (B) for varying chlorinities. Each line represents a different ab initio model. The experimental values for $\Delta^{56}Fe_{aq-eth}$ are shown (red circles) for comparison. See Tables 6 and 7. (For interpretation of the references to color in this figure legend, the reader is referred to the web version of this article.)
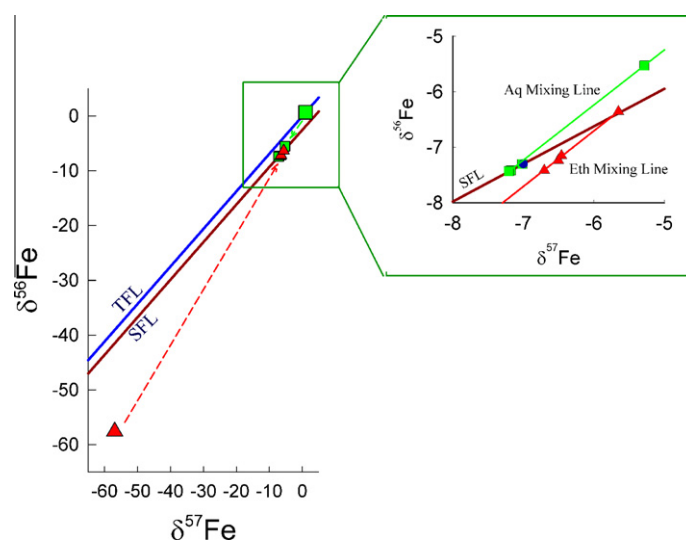
Fig. 7. Progress of aqueous and ether phases toward equilibrium in three-isotope space in the reversal experiment. The squares represent aqueous phase isotopic composition at each time step; the triangles, the ether phase. Detailed movement of each phase along its respective mixing line is shown in the inset to the right. The bulk isotopic composition (denoted by the small circle on the SFL) is at $(-7, -7.3)$. See text for discussion and Table 8.

of the separation funnel, while the volume occupied by the aqueous solution is deeper and more narrow, especially near the bottom of the funnel (Fig. A1). The aqueous phase, which contains 98% of the Fe mass (Table 8C), will most likely have a vertical gradient of mixing. Samples at $t = 20$ and 40 min were taken directly from the very bottom of the funnel, through the stopcock, without first letting some of the solution run out, in order to disturb the mixture as little as possible, resulting in aliquots of the least mixed portion of the solution. All other samples were taken as described Section 2.3. The mixing is, however, 96% complete by $t = 60$ min.

The isotopic measurements taken much later at 36 h are informative, even though controls on the experiment had lapsed and most likely there was some evaporation of the ether from the top of the separation funnel and possibly some oxidation of ferrous species. Both the aqueous and ether phases are still on the SFL, which indicates there was no external source of new iron introduced into the system (or else the bulk isotopic composition would have changed). It is also interesting that $\Delta^{56}Fe_{aq-eth}$ has moved to $-1.1‰$, slightly beyond the $-0.83‰$ separation of the forward experiment. If a small amount of ferrous iron were oxidized, then the $Fe^{2+}/Fe_{total\ aq}$ would decrease, causing $\Delta^{56}Fe_{aq-eth}$ to increase slightly (see Fig. 3). If some ether evaporated, thus increasing the Fe concentration of the ether phase, some of the ferric iron would be forced back into the aqueous phase, with similar results. It is unlikely that any HCl would evaporate from the aqueous phase since it is covered by the ether phase.

5. CONCLUSIONS

Equilibrium iron isotopic fractionation among aqueous ferric and ferrous chloride complexes was investigated to determine experimentally the effects of nonredox attributes (bond partner and coordination number) on redox fractionation. The results were compared with predictions from ab initio models. Changes in speciation resulted in a decrease in the redox fractionation of $-1.04‰$ as chlorinity increased from 1.5 M to 5.0 M, an average rate of $\sim 0.3‰/M$ [Cl$^-$], as ionic strength increased from ~ 1 to 5. The decrease in fractionation with increasing chlorinity is interpreted to result from the shift to complexes in the aqueous solution that have higher Cl/Fe ratios and smaller isotopic reduced partition function ratios ($1000\ \ln\beta$). Changes in ferric speciation had a greater effect on the redox fractionation than changes in the ferrous speciation. These experiments show that while oxidation state is the main contributor to the redox isotopic fractionation signature, in agreement with other work (e.g., Domagal-Goldman and Kubicki, 2008), nonredox attributes (such as ligands present in the solution, speciation and relative abundances, and ionic strength of the solution) can also significantly affect signatures.

We calculated four sets of ab initio models, applying UHF and hybrid DFT with different basis sets, for each ferrous chloride species for use in conjunction with the ferric chloride ab initio models from Hill and Schauble (2008). The models all show a downward trend in $1000\ \ln\beta$ as Cl$^-$ is substituted for OH$_2$ in the coordination sphere around dissolved iron. $1000\ \ln\beta$ is higher for ferric chloride species than for ferrous chloride species with the same Cl/H$_2$O stoichiometry. Theoretically estimated $1000\ \ln\alpha$ (Fe^{3+}–Fe^{2+}) decreases with increasing chlorinity, but to a lesser degree than shown by the experiments.

The immiscible liquid solvent technique may be applicable to a wider range of isotope fractionation experiments. It has advantages over precipitation methods or column elution methods in that once the system comes to equilibrium,

Table 8
Results of spiked reversal experiment. A) $\delta^{56}Fe$, $\delta^{57}Fe$, and $\Delta^{56}Fe_{aq-eth}$ of the unspiked iron solution before the ether containing spiked $FeCl_4^-$ is added. B) $\delta^{56}Fe$, $\delta^{57}Fe$, and $\Delta^{56}Fe_{aq-eth}$ of the mixed solution at 0, 20, 40, and 60 minutes after the spiked ether is added to the ether of the unspiked solution. C) Fe concentration measurements of aqueous and ether phases and bulk isotopic composition at 60 minutes. (Uncertainties are one standard error.) See text for discussion. See Fig. 7.

A. Forward Experiment (unspiked)

	$\delta^{56}Fe$	$\delta^{57}Fe$
Aqueous Phase	0.662 ± 0.013	0.962 ± 0.010
Ether Phase	1.492 ± 0.015	2.135 ± 0.023
$\Delta^{56}Fe_{aq-eth}$		-0.83 ± 0.020
Spiked Ether in Paired Exp't	-175.809	-175.045

B. Reversal Experiment (after adding spiked ether)

Mixture	0 min		20 min		40 min		60 min		(36 hours)[a]	
	$\delta^{56}Fe$	$\delta^{57}Fe$	$\delta^{56}Fe$	$\delta^{57}Fe$	$\delta^{56}Fe$	$\delta^{57}Fe$	$\delta^{56}Fe$	$\delta^{57}Fe$	$\delta^{56}Fe$	$\delta^{57}Fe$
Aqueous Phase	0.662 ± 0.013	0.962 ± 0.010	-5.529 ± 0.006	-5.287 ± 0.016	-7.416 ± 0.004	-7.177 ± 0.026	-7.302 ± 0.015	-7.017 ± 0.031	-7.433 ± 0.001	-7.205 ± 0.008
Mixed Ether Phase	-57.608[b]	-56.925[b]	$-7.416 \pm .017$	$-6.703 \pm .022$	$-7.235 \pm .004$	$-6.504 \pm .005$	$-7.15 \pm .002$	$-6.46 \pm .006$	$-6.358 \pm .008$	$-5.652 \pm .007$
$\Delta^{56}Fe_{aq-eth}$	58.270[b]		1.887 ± 0.018		-0.181 ± 0.006		-0.152 ± 0.015		-1.075 ± 0.008	

C. Fe Concentrations at 60 minutes

	[Fe] (moles/L)	Volume (ml)	% total Fe
Aqueous Phase	$0.146 \pm .003$	20	98.1
Mixed Ether Phase	0.0028 ± 0.0001	30	1.9
Bulk isotopic composition	$\delta^{57}Fe = -7.0 \pm 0.03\%_{oo}$	$\delta^{56}Fe = -7.3 \pm 0.015\%_{oo}$	

[a] See footnote 7.
[b] Calculated (based on 20 ml unspiked ether + 10 ml spiked ether); could not be measured directly since combined ether was not yet thoroughly mixed at t = 0 min.
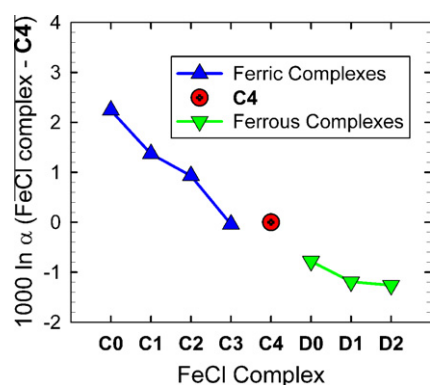
Fig. 8. Predicted Fe isotopic fractionation of ferric chloride complexes (**C***i*) and ferrous chloride complexes (**D***i*) relative to **C4**, expressed as 1000 ln α (from ab initio model B3LYP/6-311G(d)—see Table 2). 1000 ln α (**C***i*–**C4**) = 1000 ln α (**C***i*) − 1000 ln α (**C4**) and 1000 ln α (**C4**–**D***i*) = 1000 ln α (**C4**) − 1000 ln α (**D***i*).

sampling each phase does not disturb the interphase equilibrium. This experimental technique could be extended to make reversible measurements of Fe^{3+}/Fe^{2+} fractionation and fractionations associated with other inorganic and organic Fe ligands.

APPENDIX A

A.1. Ab initio models of the ferrous chloride complexes D0 ($Fe(H_2O)_6^{2+}$), D1 ($FeCl(H_2O)_5^+$), and D2 ($FeCl_2(H_2O)_4$)

A.1.1. Ab initio models—reduced partition function ratios (β factors)

Reduced partition function ratios of each relevant ferrous chloride complex were calculated from vibrational frequencies generated by electronic structure models as detailed in Section 2.4.1 and in Hill and Schauble (2008), using the standard equation from Bigeleisen and Mayer (1947).

$$\beta_{AX-X} = \prod_{i=1}^{3N-6} \left\{ (^2v_i)/(^1v_i) \right\} \left\{ \frac{\exp(-h(^2v_i)/2kT)}{1 - \exp(-h(^2v_i)/kT)} \right\}$$
$$\times \left\{ \frac{1 - \exp(-h(^1v_i)/kT)}{\exp(-h(^1v_i)/2kT)} \right\} \quad (6)$$

where β_{AX-X} is the reduced partition function ratio between species AX and a dissociated atom X (i.e., iron vapor), N is the number of atoms in the molecule, v_i is the ith vibrational frequency, h is Planck's constant, T is temperature in K, k is Boltzmann's constant, and 1 and 2 refer to molecules
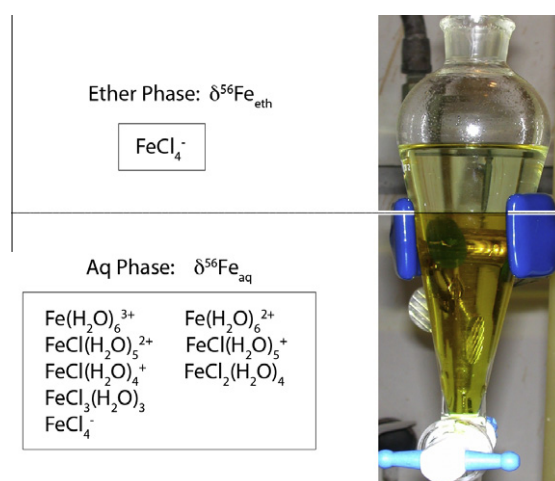

Fig. A1. Experimental setup: separation of the ether and aqueous phases in the separation funnel, showing the Fe–Cl complexes present in each phase. Adapted from Hill et al. (2009).

containing the light and heavy isotopes, respectively, of X. Unscaled[9] vibrational frequencies were used in calculating β factors for both the ferrous and the ferric species.

Vibrational frequencies for ^{56}Fe-bearing species (^{56}v) and corresponding $^{56}v/^{54}v$ ratios for ^{56}Fe- and ^{54}Fe-substituted models of each ferrous chloride complex are listed in Table B1 in Appendix B in the Electronic Annex. (For the species in the present study, only infrared- (IR-)active modes are sensitive to isotope substitution, since the iron atom does not move in IR-inactive modes.) As expected, each ^{54}v vibrational frequency is larger than its corresponding ^{56}v. IR frequencies for corresponding ferric chloride species can be found in Electronic Annex (Appendix B) of Hill and Schauble (2008).

A.1.2. Comparison of ab initio models with one another and with values from other workers

Fractionations estimated with the different electronic structure methods compare favorably with one another and with previous work (Table A3 and tables within Hill and Schauble (2008)); 1000 ln β values for the same complex vary by ⩽1.1‰. Among the ferric chloride complexes, UHF/6-31G(d) models have the highest β factors while B3LYP/6-31G(d) models generally have the lowest βs. However, among the ferrous chloride species, both the UHF/6-31G(d) and the B3LYP/6-31G(d) models have low 1000 ln β values. β factors from the DFT models with the largest basis sets, VTZ and 6-311G(d), are very similar to each other for both ferric and ferrous models. This might suggest that the results using the larger basis sets are roughly "converged," i.e., insensitive to the details of basis

---

[9] We did not scale calculated vibrational frequencies. The ab initio models underpredict the experimental frequencies. Application of the canonical scale factors would lower the frequencies and increase the difference with the experimental frequencies. See Section A.1 in Hill and Schauble (2008) for a detailed discussion of this issue. The ferric models from Hill and Schauble (2008) are also unscaled.
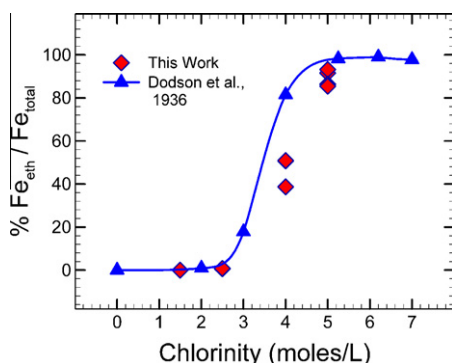
Fig. A2. Percentage of total initial ferric iron extracted into the ether for various chlorinities. The amount of ethereal iron from this work is compared to experiments from Dodson et al. (1936) in which both [H$^+$] and [Cl$^-$] were increased together (as [HCl]); in our experiments [H$^+$] = [Cl$^-$] − 2 ∗ [Fe^{2+}]. The greater dissolution of ferric Fe into the ether at similar chlorinities in the experiments of Dodson et al. shows that [H$^+$] is a limiting factor since the ethereal iron is probably dissolved as stoichiometric HFeCl$_4$ (compare with Fig. 4 in Hill et al. (2009)). The range of % Fe^{3+}/Fe$_{total}$ at each chlorinity reflects the different amounts of ferric iron available for each experiment and the small dependence of total ethereal iron upon the total amount of Fe^{3+} available; it also reflects the slightly lowered effective chlorinity in mixed solutions of ferric and ferrous chlorides since some chloride is taken up by Fe^{2+} species. See Table 4.

set choice so long as a large basis set is used, and are therefore likely to be the most accurate.

At neutral or alkaline pH, ferric hydroxides will also be present in an aqueous Fe–Cl solution. The ferric hydroxides are expected to have β factors similar to C0 (Liu and Tang, 2006; Tang and Liu, 2007), such that ligand-driven fractionation resulting from Cl$^-$ ↔ OH$^-$ substitution should be similar to the Cl$^-$ ↔ OH$_2$ effects reported here.

Reduced partition function ratios, 1000 ln β, for all models of the ferrous chloride complexes between 0 and 300 °C are listed in Table A1. Details of the optimized geometries of the models are listed in Table A2.

A.1.3. Comparison of model vibrational frequencies and bond lengths with observations

Comparing vibrational frequencies obtained through theoretical modeling with their experimental counterparts is a useful check on accuracy. However, neither is expected to be perfectly accurate. Aqueous species are approximated with in vacuo calculations, while many of the experimental spectra are from molecular salts containing the desired complex but subject to possible distortion by confinement in the crystal lattice. It is also useful to compare calculated and experimental bond lengths.

Calculated vibrational frequencies for **D0** underestimate correlated experimental frequencies, consistent with prior modeling studies (e.g., Hill and Schauble, 2008, and references therein) (Table A4). In general, the B3LYP/6-311G(d) and B3LYP/VTZ models differ from the experimental values by 9–15% while the UHF models are differ by 17–20%.
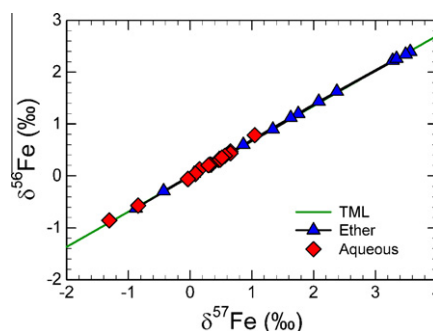

Fig. A3. Experimental values of δ^{56}Fe (‰) and δ^{57}Fe (‰) pairs from Δ^{56}Fe$_{aq–eth}$ plotted along the terrestrial mass fractionation (TML) line. This demonstrates mass-dependent fractionation and a lack of interference from Cr$^+$ in the MC-ICP-MS. See Table 5.

Calculated vibrational frequencies for **D2** are harder to correlate due to mixing and degeneracy of the modes. For example, in the B3LYP/6-311G(d) model, the vibrational mode at 204 cm^{-1} combines symmetric stretches of both Fe–O bonds and Fe–Cl bonds; other stretching frequencies also have large components of water wagging/rocking/twisting. We have tried to choose the frequencies with the strongest components of the relevant symmetric stretches for comparison with the experimental Raman frequencies (Table A4).

Table A2 shows bond lengths calculated for the ferrous chloride species. Experimental lengths are given where known. Fe–O bond lengths for **D0** from the B3LYP/6-311G(d) model are within 0.02 Å of those in an ammonium Tutton salt (Cotton et al., 1993). For **D2**, the Fe–Cl bond lengths from the B3LYP/6-311G(d) model are within 0.04 Å of those in crystalline ferrous chloride tetrahydrate; Fe–O bond lengths differ by 0.05–0.07 Å. Comparison with the longer experimental Fe–O bond length (2.59 Å) is not

Table A1

Reduced partition function ratios, 1000 ln β, calculated for all models of the ferrous complexes between 0 and 300 °C. The vibrational frequencies used in these calculations are unscaled.

T (°C)	D0	D1	D2	T (°C)	D0	D1	D2
UHF/6-31G(d)				*B3LYP/6-311G(d)*			
0	6.19	6.10	5.80	0	7.29	6.83	6.75
20	5.42	5.34	5.08	20	6.39	5.98	5.91
22	5.35	5.27	5.01	22	6.31	5.90	5.84
25	5.25	5.17	4.92	25	6.19	5.79	5.73
100	3.42	3.37	3.20	100	4.04	3.78	3.73
200	2.16	2.12	2.01	200	2.55	2.38	2.36
300	1.48	1.46	1.38	300	1.75	1.64	1.62
B3LYP/6-31G(d)				*B3LYP/VTZ*			
0	6.47	6.11	5.55	0	7.50	6.92	6.58
20	5.67	5.35	4.86	20	6.57	6.06	5.76
22	5.60	5.28	4.79	22	6.49	5.99	5.69
25	5.49	5.18	4.71	25	6.36	5.87	5.58
100	3.58	3.38	3.07	100	4.15	3.83	3.64
200	2.26	2.14	1.94	200	2.62	2.42	2.30
300	1.55	1.47	1.33	300	1.80	1.66	1.58

Table A2
Ab initio and experimental (when available) bond lengths of the ferrous chloride ab initio models.[1] Lengths are in Ångstroms.

Ferrous Chloride Complex	Ab initio model	Fe-O bond length	Fe-Cl bond length	Exp't Fe-O bond length	Exp't Fe-Cl bond length
D0 = $[Fe(H_2O)_6^{2+}]$				2.143×2[2]	
				2.136×2	
				2.098×2	
	B3LYP/6-311G(d)	2.150×2			
		2.149×2			
		2.119×2			
	B3LYP/6-31G(d)	2.156×2			
		2.149×2			
		2.113×2			
	B3LYP/VTZ	2.139×1			
		2.138×3			
		2.111×2			
	UHF/6-31G(d)	2.186×6			
D1 = $[FeCl(H_2O)_5^{+}]$					
	B3LYP/6-311G(d)	2.238×2	2.284		
		2.167×2			
		2.113×1			
	B3LYP/6-31G(d)	2.283	2.282		
		2.293			
		2.181			
		2.182			
		2.113			
	B3LYP/VTZ	2.228×2	2.324		
		2.168×2			
		2.102×1			
	UHF/6-31G(d)	2.283	2.282		
		2.293			
		2.181			
		2.182			
		2.113			
D2 = $[FeCl_2(H_2O)_4]$				2.09×2[3]	2.38×2[3]
				2.59×2[4]	
		2.156			
	B3LYP/6-311G(d)	2.157	2.417		
		2.146	2.414		
		2.145			
	B3LYP/6-31G(d)	2.224×2	2.382		
		2.274×2	2.376		
	B3LYP/VTZ	2.159			
		2.168	2.387		
		2.191	2.541		
		2.156			
	UHF/6-31G(d)	2.256×4	2.423×2		

[1] Bond lengths of the ab initio models usually differ in the fifth or sixth decimal place resulting in C1 symmetries.
[2] Cotton et al., 1993 – ammonium Tutton salt.
[3] Penfold & Grigor, 1959 – FeCl₂ (H₂O)₄ - ferrous chloride tetrahydrate crystals.
[4] Penford & Grigor, 1959 (as above); exceptionally long & probably distorted, due to its position in the crystal lattice.

useful since the bond is most likely distorted and weakened by its position in the crystalline structure (Gamo, 1961).

A.1.4. Comparison of theoretical models with experimental redox data from other workers

In our previous work (Hill and Schauble, 2008—Section 4.4 and Table 5), we compared theoretical fractionations with published experiments. It is useful to revisit the two experiments (Johnson et al., 2002; Welch et al., 2003) that measured fractionation between aqueous ferric and ferrous chlorides now that we have ab initio models for the ferrous chlorides as well as the ferric chlorides.

Table A3
Comparison of 1000 ln β for different models of **D0** ($Fe(H_2O)_6^{2+}$) at 20 °C.

	$Fe(H_2O)_6^{2+}$
UHF/6-31G(d)	5.42
B3LYP/6-31G(d)	5.68
B3LYP/6-311G(d)	6.39
B3LYP/VTZ	6.57
B3LYP/LANL2DZ with ECP (Hill and Schauble, 2008)	6.7
B3LYP/VTZ without PCM (Anbar et al., 2005)	6.76
MUBFF (Schauble et al., 2001)	6.42

Table A4
Comparison of experimental and ab initio model vibrational frequencies for **D0** and **D2** (values in cm^{-1}).

Exp. vib. freq.	Mode	UHF/6-31G(d)	B3LYP/6-31G(d)	B3LYP/6-311G(d)	B3LYP/VTZ
_D0_					
389[a]	ν_3	310.6536	313.3644	340.4837	339.4937
		322.0718	324.2500	342.4934	344.4237
		322.0722	338.2649	354.2695	374.3216
_D2_					
189[b]	Fe–Cl stretches	206.99	201.5311	203.7793	185.8307
192		281.54	212.2937		
213	Fe–O stretches	206.99	212.2937	203.7793	185.8307
310		281.54	302.9872	316.4582	316.9385

[a] X-ray—aquo complex ions in FeSiF$_6$·6H$_2$O (Nakagawa and Simanouchi, 1964).
[b] Raman—FeCl$_2$·4(H$_2$O) crystal (Cariati et al., 1984).

Table A5
Comparison of experimental values from other workers vs. theoretical predictions of aqueous Fe^{3+}/Fe^{2+} fractionation (in ‰) at very low chlorinities. Experimental values of redox fractionation in aqueous solution are compared to predicted fractionations calculated using ab initio models of ferric chlorides from Hill and Schauble (2008) and of ferrous chlorides from this work, using three different speciation models from the original papers. Ab initio models predict a small average decrease in 1000 ln β of ~0.3–0.5‰ as chlorinity increases to 111 mM, while experiments have not detected any change (adapted from Table 8 in Hill and Schauble (2008)).

mM Cl$^-$	Exp.	B3LYP/VTZ predictions			B3LYP/6-31G(d) predictions		
		GWB	PHREEQC	MINEQL+	GWB	PHREEQC	MINEQL+
Johnson et al. (2002)							
22	2.75 ± 0.15	2.93	2.84	2.79	3.18	3.09	3.05
		WATEQ	PHREEQ	MINTEQ	WATEQ	PHREEQ	MINTEQ
Welch et al. (2003)							
0	3.02 ± 0.14	2.76	2.71	2.77	3.14	3.18	3.19
11	3.05 ± 0.17	2.66	2.62	2.84	3.06	3.09	3.10
111	2.92 ± 0.08	2.26	2.38	2.45	2.85	2.75	2.76

The overall fractionation between the ferric chlorides (A) and the ferrous chlorides (B) can be calculated as

$$1000 \ln \alpha_{(A-B)} = \sum (X_i * 1000 \ln \beta_i)_A - \sum (X_i * 1000 \ln \beta_i)_B \tag{7}$$

where X_i is mole fraction of each Fe–Cl complex at the given chlorinity and β_i is the β factor for that complex. In Hill and Schauble, we used the calculated 1000 ln β of **D0** as a rough stand in for **D1**, **D2**, and ferrous hydroxides, and of **C0** as a stand in for ferric hydroxides. Anbar et al.'s (2005) DFT without PCM value for **D0** was adopted for comparison with our B3LYP/VTZ models. In our new calculations we use values from the present work for **D0**, **D1**, and **D2**. Hydroxides are still assumed to be equivalent to **C0** or **D0** as before. The two sets of experiments are compared in Table A5 (compare with Table 8 in Hill and Schauble). Since there is so little **D1** and no **D2** at the low chlorinities of the experiments, the resultant change in the predicted fractionation is within 0.01‰ of the previous prediction with B3LYP/6-31G(d) models. The predicted values from B3LYP/VTZ models shift by about 0.05‰ for the low chlorinity experiments in Welch et al. and about 0.2‰ for the slightly higher chlorinity experiment in Johnson et al., mainly due to the difference in our 1000 ln β for **D0** compared to the Anbar et al. model (see Table A3). The overall

results of the predicted ferric–ferrous fractionation from the new ab initio models, as in the previous calculations, include a decrease in the redox fractionation of 0.3–0.5‰ with increasing chlorinity (Table A5), which is not seen in the experiments. (See Hill and Schauble for a more detailed discussion of the Welch et al. and Johnson et al. experiments.) See Section 4.2 for discussion of redox fractionation at very low chlorinities.

APPENDIX B. SUPPLEMENTARY DATA

Supplementary data associated with this article can be found, in the online version, at doi:10.1016/j.gca.2010.08.038.

REFERENCES

Amils R., González-Toril E., Fernández-Remolar D., Gómez F., Aguilera A., Rodríguez N., Malki M., García-Moyano G., Fairén A. G., de la Fuente V. and Sanz J. L. (2007) Extreme environments as Mars terrestrial analogs: the Rio Tinto case. _Planet. Space Sci._ **55**, 370–381.

Anbar A. D., Roe J. E., Barling J. and Nealson K. H. (2000) Non-biological fractionation of iron isotopes. _Science_ **288**, 126–128.

Anbar A. D., Jarzecki A. A. and Spiro T. G. (2005) Theoretical investigation of iron isotope fractionation between Fe(H$_2$O)$_6^{3+}$

and $Fe(H_2O)_6^{2+}$: implications for iron stable isotope geochemistry. *Geochim. Cosmochim. Acta* **69**, 825–837.

Apted M. J., Waychunas G. A. and Brown G. E. (1985) Structure and specification of iron complexes in aqueous solutions determined by X-ray absorption spectroscopy. *Geochim. Cosmochim. Acta* **49**, 2081–2089.

Beard B. L. and Johnson C. M. (2004) Fe isotope variations in the modern and ancient earth and other planetary bodies. In *Geochemistry of Non-Traditional Stable Isotopes Reviews in Mineralogy & Geochemistry*, vol. 55, pp. 319–357.

Becke A. D. (1993) Density-functional thermochemistry: III. The role of exact exchange. *J. Chem. Phys.* **98**, 5648–5652.

Best S. P., Beattie J. K. and Armstrong R. S. (1984) Vibrational spectroscopic studies of trivalent hexa-aqua-cations: single-crystal Raman spectra between 275 and $1200 \, cm^{-1}$ of the caesium alums of titanium, vanadium, chromium, iron, gallium, and indium. *J. Chem. Soc., Dalton Trans.* **12**, 2611–2624.

Bethke C. M. (1996) *Geochemical Reaction Modeling Concepts and Applications*. Oxford University Press, New York.

Bigeleisen J. and Mayer M. G. (1947) Calculation of equilibrium constants for isotopic exchange reactions. *J. Chem. Phys.* **15**, 261–267.

Bjerrum J. and Lukes I. (1986) The iron(III)–chloride system. A study of the stability constants and of the distribution of the tetrachloro species between organic solvents and aqueous chloride solutions. *Acta Chem. Scand. Ser. A: Phys. Inorg. Chem.* **15**, 31–40.

Bowen B. B., Benison K. C., Oboh-Ikuenobe F. and Mormile M. (2007) Hematite concretions from modern acid saline lake sediments as geochemical and astrobiological tombs. *Lunar Planet. Sci. Seventh Int. Conf. Mars.* #3175 (abstr.).

Bromley L. A. (1973) Thermodynamic properties of strong electrolytes in aqueous solution. *AIChE J.* **19**, 313–320.

Cariati F., Masserano F., Martini M. and Spinolo G. (1984) Raman studies of $NiX_2 \cdot 6H_2O$ and $FeCl_2 \cdot 4H_2O$. *J. Raman Spectrosc.* **20**, 773–777.

Cotton S. A. and Gibson J. F. (1971) Spectroscopic studies of some aquo-complexes of iron (III) and indium (III). *Inorg. Phys. Theor.: J. Chem. Soc. A* **11**, 1693–1696.

Cotton F. A., Daniels L. M., Murillo C. A. and Quesada J. F. (1993) Hexaaqua dipositive ions of the 1st transition series—new and accurate structures—expected and unexpected trends. *Inorg. Chem.* **32**, 4861–4867.

Delmelle P. and Bernard A. (1994) Geochemistry, mineralogy, and chemical modeling of the acid crater lake of Kawah-Ijen Volcano, Indonesia. *Geochim. Cosmochim. Acta* **58**, 2445–2460.

Dodson R. W., Forney G. J. and Swift E. H. (1936) The extraction of ferric chloride from hydrochloric acid solutions by isopropyl ether. *J. Am. Chem. Soc.* **58**, 2573–2577.

Domagal-Goldman S. D. and Kubicki J. D. (2008) Density functional theory predictions of equilibrium isotope fractionation of iron due to redox changes and organic complexation. *Geochim. Cosmochim. Acta* **72**, 5201–5216.

Frisch M. J., Trucks G. W., Schlegel H. B., Scuseria G. E., Robb M. A., Cheeseman J. R., Montgomery, Jr., J. A., Vreven T., Kudin K. N., Burant J. C., Millam J. M., Iyengar S. S., Tomasi J., Barone V., Mennucci B., Cossi M., Scalmani G., Rega N., Petersson G. A., Nakatsuji H., Hada M., Ehara M., Toyota K., Fukuda R., Hasegawa J., Ishida M., Nakajima T., Honda Y., Kitao O., Nakai H., Klene M., Li X., Knox J. E., Hratchian H. P., Cross J. B., Adamo C., Jaramillo J., Gomperts R., Stratmann R. E., Yazyev O., Austin A. J., Cammi R., Pomelli C., Ochterski J. W., Ayala P. Y., Morokuma K., Voth G. A., Salvador P., Dannenberg J. J., Zakrzewski V. G., Dapprich S., Daniels A. D., Strain M. C., Farkas O., Malick D. K., Rabuck A. D., Raghavachari K., Foresman J. B., Ortiz J. V., Cui Q.,

Baboul A., Clifford S., Cioslowski J., Stefanov B. B., Liu G., Liashenko A., Piskorz P., Komaromi I., Martin R. L., Fox D. J., Keith T., Al-Laham M. A., Peng C. Y., Nanayakkara A., Challacombe M., Gill P. M. W., Johnson B., Chen W., Wong M. W., Gonzalez C. and Pople J. A. (2004) *Gaussian 03, Revision C.02*. Gaussian, Inc., Wallingford, CT.

Fujii T., Moynier F., Telouk P. and Albarède F. (2006) Isotope fractionation of iron(III) in chemical exchange reactions using solvent extraction with crown ether. *J. Phys. Chem. A* **110**, 11108–11112.

Gamo I. (1961) Infrared absorption spectra of water of crystallization in ferrous chloride tetrachloride crystal. *Bull. Chem. Soc. Jpn.* **34**, 1433–1435.

Heinrich C. A. and Seward T. M. (1990) A spectrophotometric study of aqueous iron (II) chloride complexing from 25 to 200 °C. *Geochim. Cosmochim. Acta* **5**, 2207–2221.

Hill P. S. and Schauble E. A. (2008) Modeling the effects of bond environment on equilibrium iron isotope fractionation in ferric aquo-chloro complexes. *Geochim. Cosmochim. Acta* **72**, 1939–1958.

Hill P. S., Schauble E. A., Shahar A., Tonui E. and Young E. D. (2009) Experimental studies of equilibrium iron isotope fractionation in ferric aquo-chloro complexes. *Geochim. Cosmochim. Acta* **73**, 2366–2381.

Hofmann A., Bekker A., Rouxel O., Rumble D. and Master S. (2009) Multiple sulphur and iron isotope composition of detrital pyrite in Archaean sedimentary rocks: a new tool for provenance analysis. *Earth Planet. Sci. Lett.* **286**, 436–445.

Inada Y. and Funahashi S. (1999) Equilibrium and structural study of chloro complexes of iron(III) in acidic aqueous solution by means of X-ray absorption spectroscopy. *Z. Naturforsch. B: Chem. Sci.* **54**, 1517–1523.

Jamieson H. E., Robinson C., Alpers C. N., Nordstrom D. K., Poustovetov A. and Lowers H. A. (2005) The composition of coexisting jarosite-group minerals and water from the Richmond mine, Iron Mountain, California. *Can. Mineral.* **43**, 1225–1242.

Johnson C. M., Beard B. L. and Roden E. E. (2008) The Iron isotope fingerprints of redox and biogeochemical cycling in modern and ancient Earth. *Annu. Rev. Earth Planet. Sci.* **36**, 457–493.

Johnson C. M., Skulan J. L., Beard B. L., Sun H., Nealson K. H. and Braterman P. S. (2002) Isotopic fractionation between Fe(III) and Fe(II) in aqueous solutions. *Earth Planet. Sci. Lett.* **195**, 141–153.

Lee M. S. (2004) Use of the Bromley equation for the analysis of ionic equilibria in mixed ferric and ferrous chloride solutions at 25 °C. *Metall. Mater. Trans. B* **37B**, 173–179.

Lee M. S., Ahn J. G. and Oh Y. J. (2003) Chemical model of the $FeCl_3$–HCl–H_2O solutions at 25 °C. *Mater. Trans.* **44**, 957–961.

Lind M. D. (1967) Crystal structure of ferric chloride hexahydrate. *J. Chem. Phys.* **47**, 990–993.

Liu W., Etschmann B., Foran G., Shelley M. and Brugger J. (2007) Deriving formation constants for aqueous metal complexes from XANES spectra: Zn^{2+} and Fe^{2+} chloride complexes in hypersaline solutions. *Am. Mineral.* **92**, 761–770.

Liu Y. and Tang M. (2006) Iron isotopic fractionations between species in solution—from ab initio quantum chemistry calculations. *Geochim. Cosmochim. Acta Suppl.* **70**, 367 (abstr.).

Magini M. and Radnai T. (1979) X-ray diffraction study of ferric chloride solutions and hydrated melt. Analysis of the iron (III)–chloride complexes formation. *J. Chem. Phys.* **71**, 4255–4262.

Mahon K. I. (1996) The New "York" regression: application of an improved statistical method to geochemistry. *Int. Geol. Rev.* **38**, 293–303.

Mathews A., Goldsmith J. R. and Clayton R. N. (1983) On the mechanisms and kinetics of oxygen isotope exchange in quartz and feldspars at elevated temperatures and pressures. *GSA Bull.* **94**, 396–412.

Matsuhisa Y., Goldsmith J. R. and Clayton R. N. (1978) Mechanisms of hydrothermal crystallization of quartz at 250 °C and 15 kbar. *Geochim. Cosmochim. Acta* **42**, 173–182.

Murata K. and Irish D. E. (1988) Raman studies of the hydrated melt of FeCl$_3$∗6H$_2$O. *Geochim. Cosmochim. Acta* **44A**, 739–743.

Murata K., Irish D. E. and Toogood G. E. (1989) Vibrational spectral studies of solutions at elevated temperatures and pressures: II. A Raman spectral study of aqueous iron(III) chloride solutions between 25 and 300 °C. *Can. J. Chem.* **67**, 517–524.

Nachtrieb N. H. and Conway J. G. (1948) The extraction of ferric chloride by isopropyl ether: I. *J. Am. Chem. Soc.* **70**, 3547–3552.

Nachtrieb N. H. and Fryxell R. E. (1948) The extraction of ferric chloride by isopropyl ether: II. *J. Am. Chem. Soc.* **70**, 3552–3557.

Nakagawa I. and Simanouchi T. (1964) Infrared absorption spectra of aquo complexes and the nature of co-ordination bonds. *Spectrochim. Acta* **20**, 429–439.

Penfold B. R. and Grigor J. A. (1959) The crystal structure of iron(II) chloride tetrahydrate. *Acta Crystallogr.* **12**, 850–854.

Polyakov V. B. and Mineev S. D. (2000) The use of Mössbauer spectroscopy in stable isotope geochemistry. *Geochim. Cosmochim. Acta* **64**, 849–865.

Rabinowitch E. and Stockmayer W. H. (1942) Association of ferric ions with chloride, bromide and hydroxyl ions (a spectroscopic study). *J. Am. Chem. Soc.* **64**, 335–347.

Rassolov V. A., Pople J. A., Ratner M. A. and Windus T. L. (1998) 6-31G(d) basis set for atoms K through Zn. *J. Chem. Phys.* **109**, 1223–1229.

Rouxel O. J., Bekker A. and Edwards K. J. (2005) Iron isotope constraints on the Archean and Paleoproterozoic ocean redox state. *Science* **307**, 1088–1091.

Sandell E. B. (1944) *Colorimetric Determination of Traces of Metals.* Interscience Publishers, New York.

Schäfer A., Horn H. and Ahlrichs R. (1992) Fully optimized contracted Gaussian-basis sets for atoms Li to Kr. *J. Chem. Phys.* **97**, 2571–2577.

Schauble E. A. (2004) Applying stable isotope fractionation theory to new systems. In *Geochemistry of Non-Traditional Stable Isotopes: Reviews in Mineralogy & Geochemistry*, vol. 55, pp. 65–111.

Schauble E. A., Rossman G. R. and Taylor, Jr., H. P. (2001) Theoretical estimates of equilibrium Fe-isotope fractionations from vibrational spectroscopy. *Geochim. Cosmochim. Acta* **65**, 2487–2497.

Shahar A., Manning C. E. and Young E. D. (2008) Equilibrium high-temperature Fe isotope fractionation between fayalite and magnetite: an experimental calibration. *Earth Planet. Sci. Lett.* **268**(3–4), 330–338.

Shamir J. (1991) Raman and infrared spectra of the FeCl$_6$$^{3-}$ anion: comparison of MCl4 and MCl6 vibrational frequencies. *J. Raman Spectrosc.* **22**, 97–99.

Sharma S. K. (1974) Raman study of ferric chloride hexahydrate and ferric chloride hexadeuterate in crystalline, molten and glassy states. *J. Non-Cryst. Solids* **15**, 83–95.

Stookey L. L. (1970) Ferrozine—a new spectrophotometric reagent for iron. *Anal. Chem.* **42**, 779–781.

Tang M. and Liu Y. (2007) Re-evaluation of the equilibrium fe isotope fractionation between Fe^{3+}(H$_2$O)$_6$ and Fe^{3+}(H$_2$O)$_6$ in aqueous solution. *Geochim. Cosmochim. Acta Suppl.* **71**, A1000 (abstr.).

Tosca N. J., McLennan S. M., Clark B. C., Grotzinger J. P., Hurowitz J. A., Knoll A. H., Schröder C. and Squyres S. W. (2005) Geochemical modeling of evaporation processes on Mars: insight from the sedimentary record at Meridiani Planum. *Earth Planet. Sci. Lett.* **240**, 122–148.

Vollier E., Inglett P. W., Hunter K., Roychoudhury A. N. and VanCappellen P. (2000) The ferrozine method revisited: Fe(II)/Fe(III) determination in natural waters. *Appl. Geochem.* **15**, 785–790.

Welch S. A., Beard B. L., Johnson C. M. and Braterman P. S. (2003) Kinetic and equilibrium Fe isotope fractionation between aqueous Fe(II) and Fe(III). *Geochim. Cosmochim. Acta* **67**, 4231–4250.

Yamaguchi K. E., Johnson C. M., Beard B. L., Beukes N. J., Gutzmer J. and Ohmoto H. (2007) Isotopic evidence for iron mobilization during Paleoproterozoic lateritization of the Hekpoort paleosol profile from Gaborone, Botswana. *Earth Planet. Sci. Lett.* **256**, 577–587.

Yamaguchi K. E. and Ohmoto H. (2006) Geochemical and isotopic constraints on the origin of Paleoproterozoic red shales of the Gamagara/Mapedi Formation, Postmasburg Group, South Africa. *S. Afr. J. Geol.* **109**, 123–138.

Young E. D., Galy A. and Nagahara H. (2002) Kinetic and equilibrium mass-dependent fractionation laws in nature and their geochemical and cosmochemical significance. *Geochim. Cosmochim. Acta* **66**, 1095–1104.

Zhao R. and Pan P. (2001) A spectrophotometric study of Fe(II)–chloride complexes in aqueous solutions from 10 to 100 °C. *Can. J. Chem.* **79**, 131–144.

Associate editor: Clark M. Johnson